



# Pinecone-derived porous activated carbon for high performance all-solid-state electrical double layer capacitors fabricated with flexible gel polymer electrolytes

Md. Yasir Bhat, Nitish Yadav, S.A. Hashmi\*

Department of Physics and Astrophysics, University of Delhi, Delhi, 110007, India



## ARTICLE INFO

### Article history:

Received 26 October 2018

Received in revised form

21 February 2019

Accepted 23 February 2019

Available online 25 February 2019

### Keywords:

Bio-waste pinecone

Activated carbon

Electrical double layer capacitor

Gel polymer electrolyte

Plastic crystals

## ABSTRACT

We report a novel configuration of electrical double layer capacitors (EDLCs), fabricated with porous activated carbon electrodes derived from bio-waste pinecone and plastic crystals-based gel polymer electrolytes. Different activated carbons have been produced by activating raw pinecone powder employing different amount of activating agent  $\text{ZnCl}_2$ . Optimization of morphology, structure and porosity parameters of activated carbons has been performed by scanning electron microscopy, x-ray diffraction, Raman and porosity analyses. Mixed (micro- and meso-) porous interiors in activated carbon show optimum characteristics of EDLCs. Gel polymer electrolyte comprising mixture of non-ionic plastic crystal and organic ionic plastic crystal (succinonitrile and 1-ethyl-1-methyl pyrrolidinium bis(trifluoromethyl sulfonyl)imide, respectively) entrapped in poly(vinylidene fluoride-co-hexafluoropropylene) has been found suitable to fabricate EDLCs owing to their flexible nature, high ionic conductivity ( $\sigma \sim 1.53 \times 10^{-3} \text{ S cm}^{-1}$  at room temperature) and wide enough electrochemical stability window, ESW ( $\sim 3.1 \text{ V}$  versus Ag). Addition of Li-salt in the gel polymer electrolyte improves the electrochemical properties ( $\sigma \sim 2.87 \times 10^{-3} \text{ S cm}^{-1}$  and ESW  $\sim 3.8 \text{ V}$ ) and found to influence the performance of the EDLCs, particularly, the specific power, significantly. The EDLC cell with Li-salt containing electrolyte offers higher values of specific capacitance, energy and power ( $\sim 255 \text{ F g}^{-1}$ ,  $\sim 20 \text{ Wh kg}^{-1}$  and  $\sim 55.7 \text{ kW kg}^{-1}$ , respectively) than the cell with electrolyte without Li-salt ( $\sim 244 \text{ F g}^{-1}$ ,  $\sim 19 \text{ Wh kg}^{-1}$  and  $\sim 39.3 \text{ kW kg}^{-1}$ , respectively). The EDLC (with Li-salt electrolyte) exhibits 96–100% Coulombic efficiency and almost stable specific capacitance for  $\sim 20,000$  charge-discharge cycles after only  $\sim 11\%$  initial fading. The capacitor gives stable performance for a wide temperature range from  $-30$  to  $90^\circ\text{C}$ .

© 2019 Elsevier Ltd. All rights reserved.

## 1. Introduction

'Electrical double layer capacitors (EDLCs)' is one of the important classes of electrochemical capacitors (ECs), also referred as Supercapacitors, which have attracted global attention due to many advantageous properties as energy storage devices, such as high-power density, long cycle life, fast charge-discharge rate and simple configuration [1–3]. EDLCs/supercapacitors are globally used in a variety of applications including consumer electronics, power supplies, escalators, electrical vehicles and different pulsing technologies and industrial power [4,5]. A variety of carbonaceous

porous materials, including activated carbon [1–15], carbon nanotubes (CNTs) [16,17], carbon aerogels [18,19], carbon nanofibres (CNFs) [20,21], carbide-derived carbons [22,23] and graphene-based materials [24–27], have demonstrated their potential as electrodes in EDLC fabrication. Porous activated carbons (ACs) are still considered to be most attractive candidates as EDLC electrodes owing to their advantageous features such as high specific surface area, tuneable porosity providing facile pathways for easy accessibility and transport of electrolyte ions, high electrical conductivity, and excellent electrochemical stability [1–4,17]. To a certain extent, chemical inertness is another important feature of porous carbon electrodes of EDLCs, responsible for electrostatic storage of translational charges at the electrode-electrolyte interfaces [1–5].

Coal, petroleum and their derivatives are traditionally used to produce ACs, which involves expensive and environmentally hazardous methods of preparation [28–31]. In the recent past,

\* Corresponding author.

E-mail addresses: [sahashmi@physics.du.ac.in](mailto:sahashmi@physics.du.ac.in), [hashmisa2002@yahoo.co.in](mailto:hashmisa2002@yahoo.co.in) (S.A. Hashmi).

researchers have given attention towards the preparation of activated carbons from biomasses/bio-wastes as cost-effective and eco-friendly alternatives [4,9–14,32–35]. Different biomasses/bio-wastes including coconut shells, coffee beans, almond shells, peanut shells, sunflower seed shells, rubber wood sawdust, bamboo, rice husk, waste paper, dead leaves, seaweeds, etc. are reported as potential carbon precursors to produce ACs for various applications including sustainable and scalable supercapacitors [6,12,32–41]. Different methods have been reported to prepare ACs from biomasses/biomasses namely hydrothermal process [42], chemical vapour deposition (CVD) [43], direct pyrolysis [38], wet chemistry techniques such as sol-gel process [39], gas solid displacement reaction [44], etc. and each method of preparation has its merits and demerits. The classical synthesis route of ACs via pyrolysis of biomasses followed by chemical/physical activation is still a viable method as it is easy and cost-effective route on commercial scale [42].

In the present work, we have produced the porous activated carbon from a bio-waste pinecone to employ as electrode material for EDLCs. Pines are coniferous trees, which belong to the genus *Pinus* family of the Pinaceae, grow up to 50 m in height [45]. Such trees possess dark green needles and 5–10 cm length cones with rounded scales. A large number of cones are produced throughout the world and a large proportion of them are waste. Some pine plantations are especially grown for the paper and pulp industries. The cones of pines primarily comprise cellulose, lignin and resins containing different organic compounds [46,47]. These components play important role in creating different types of porosity when evaporated during carbonisation and chemical/physical activation processes [15]. Some reports exist on pinecone-based porous carbons for their extensive application as bio-sorbent of dyes and metals from waste aqueous solutions and improved nitrate uptake [48–50]. A few studies are reported to employ activated carbon, produced from pine products, as supercapacitor electrodes, which are tested in different liquid electrolytes [51–53].

Most of the reported supercapacitors including EDLCs are tested in and fabricated with aqueous and organic liquid electrolytes, e.g. aqueous solution of  $\text{Na}_2\text{SO}_4$ ,  $\text{H}_2\text{SO}_4$ , etc., and solution of tetraethylammonium tetrafluoroborate  $\text{TEABF}_4$ ,  $\text{LiBF}_4$ , etc. in acetone, propylene carbonate (PC), etc. [2,3,5,54–58]. These electrolytes show many adverse performances including corrosion of electrodes and current collectors, electrolyte leakage, instability due to their high volatility, difficulty in miniaturization, and limitation in transportability. Flammability is another problem of organic liquid electrolytes, which is related to safety issues [58]. Few issues related to chemical/electrochemical/thermal instabilities and most importantly safety concerns related to flammability of the liquid electrolytes are tackled using ionic liquids (ILs) or salt solutions of ILs as capacitor electrolytes [59,60]. Supercapacitors/EDLCs of present generation have started relying on gel polymer electrolytes (GPEs), in which liquid electrolytes are entrapped in polymeric networks e.g. poly vinyl alcohol (PVA), poly(methyl methacrylate) (PMMA), poly(vinylidene fluoride) (PVdF), poly(vinylidene fluoride-co-hexafluoropropylene) (PVdF-HFP), etc. [12,17,24,25,61,62]. GPEs possess profitable properties including liquid-like electrochemical properties and quasi-solid-like flexible mechanical properties [61,62]. Among their different types, IL-incorporated-GPEs are of recent choices, as they offer various supplementary properties like high ionic conductivity, sufficient electrochemical potential window, excellent mechanical and thermal stability, and safety due to non-flammability [61–63].

Plastic crystals electrolytes, a recently introduced class of materials, are considered as solid-state electrolytes that attract attention of researchers due to their properties including liquid-like nature, and solid-like physical appearance and mechanical

behavior [64]. Plastic crystals are subdivided in two fascinating classes namely: (i) organic ionic plastic crystals (OIPCs), which are basically aliphatic or heterocyclic organic salts (e.g., *N*-ethyl-*N*-methylpyrrolidinium tetrafluoroborate,  $[\text{C}_2\text{mpyr}][\text{BF}_4]$ , *N*-ethyl-*N*-methylpyrrolidinium bis(trifluoromethane sulfonyl) imide  $[\text{C}_2\text{mpyr}][\text{TFSI}]$ , etc.) showing plastic crystalline nature in a certain temperature range [64,65], and (ii) non-ionic plastic crystals, the most popular one is succinonitrile (SN) [66,67]. OIPCs and SN offer fast ion conductivity, particularly, for different target ions ( $\text{Li}^+$ ,  $\text{Na}^+$ ,  $\text{Mg}^{2+}$ , etc.), when they are added with low concentration of foreign salts [64–68]. For example, SN has been established as universal matrix, which has capability to accommodate various types of salts forming different fast ion conducting electrolytes, suitable for application in batteries [68]. Such fast ion conducting electrolytes have been demonstrated for OIPCs also when added with different salts [64]. When these plastic crystal/salt mixtures are entrapped in suitable host polymers e.g. PVdF-HFP, etc., they form unique composition of gel polymer electrolytes (GPEs). There exist various reports on potential polymer-based electrolytes/GPEs comprising OIPCs or SN, added with suitable salts, entrapped in different polymeric networks including PEO, PVdF-HFP, etc. [24,25,36,67–73]. These electrolytes have found their way in potential applicability in various devices including supercapacitors [24,25,36,68,72,73].

In this work, studies are presented on sustainable activated porous carbons, produced by carbonizing a bio-waste pinecone powder followed by activation employing different amount of activating agent  $\text{ZnCl}_2$ . Detailed morphological, structural and porosity analyses have been performed to optimise the carbon powder by scanning electron microscopy (SEM), X-ray diffraction (XRD), Raman spectroscopy and  $\text{N}_2$ -adsorption-desorption measurements. Electrical double layer capacitors (EDLCs) have been fabricated by using electrodes containing optimized activated carbon and GPE comprising mixture of OIPC (1-ethyl-1-methylpyrrolidinium bis(trifluoromethylsulfonyl) imide, EMPTFSI) and non-ionic plastic crystal (SN), immobilised in host polymer PVdF-HFP. Different electrochemical techniques, namely; cyclic voltammetry (CV), electrochemical impedance spectroscopy (EIS), and galvanostatic charge-discharge (GCD) tests have been applied to evaluate the performance of EDLCs. Substantial improvement in the performance characteristics has been found on employing lithium salt (LiTFSI) incorporated GPE in EDLCs.

## 2. Experimental

### 2.1. Preparation of AC electrodes

Porous activated carbon powders were prepared from bio-waste pinecone following the chemical and physical activation processes [74], as schematically shown in Fig. 1. The steps of processing are given as follows. First, the raw pinecone was grounded thoroughly to prepare a fine powder. The pinecone powder was then added with an activating agent zinc chloride in different ratios (1:1, 1:2, 1:3 and 1:5 w/w) for chemical activation. The mixtures were prepared in the form of slurries with de-ionized water by thorough mixing in a mortar and pestle, followed by drying overnight at  $\sim 110^\circ\text{C}$  in vacuum. The mixtures, so obtained, were then heated by increasing the temperature from room temperature to  $800^\circ\text{C}$  at a heating rate of  $5^\circ\text{C min}^{-1}$  under the constant flow of nitrogen gas. The materials were then exposed to the constant flow of  $\text{CO}_2$  gas, maintaining the temperature  $\sim 800^\circ\text{C}$  for 2 h for physical activation. It may be noted that the physical activation, after the chemical activation, results in widening the pores in carbon materials [74,75]. After cooling slowly at room temperature, the powders were washed first by HCl to dissolve and remove residual zinc



Fig. 1. Schematic diagram of the preparation of activated carbon from biomass pinecone.

compounds, followed by washing them with hot de-ionized water to wash out chloride ions. The resulting activated carbon powders were dried overnight at  $\sim 110^\circ\text{C}$  in vacuum. All the AC powders were stored in moisture-free atmosphere. The AC powders were physically characterized and optimized for application as electrode material in EDLCs.

Electrodes for EDLCs were prepared by mixing optimized AC powder, conductive additive (acetylene black, AB) and a binder (PVdF-HFP), maintaining their ratio of 80:10:10 (w/w). A slurry of this mixture was prepared by adding acetone and mixed thoroughly in agate mortar and pestle. The slurry was then finely spread on flexible graphite sheets ( $\sim 250\ \mu\text{m}$  thick, Nickunj Eximp Enterprises, India) and dried at  $\sim 100^\circ\text{C}$  in vacuum to obtain EDLC electrodes. The size of the electrodes for EDLC fabrication was kept to  $1 \times 1\ \text{cm}^2$ . Mass of AC powder, loaded in electrodes, was  $0.72\text{--}0.75\ \text{mg cm}^{-2}$  [76,77].

## 2.2. Preparation of GPEs

The co-polymer PVdF-HFP (average MW  $\approx 400,000\ \text{g mol}^{-1}$ ), succinonitrile (SN, 99%), 1-ethyl-1-methylpyrrolidinium bis(trifluoromethylsulfonyl)imide (EMPTFSI, 99%) and lithium bis(trifluoromethylsulfonyl)imide (LiTFSI,  $\geq 99\%$ ) were procured from Sigma-Aldrich. These chemicals were vacuum dried for 12 h at room temperature prior to use. For the GPE film preparation, 5 mol % of EMPTFSI was added in SN and mixed thoroughly. The EMPTFSI/SN solution was then added to the acetone solution of PVdF-HFP. Another composition of this mixture was prepared with lithium salt, LiTFSI. For that, 1 M LiTFSI was added to EMITFSI/SN solution and then dispersed in acetone solution of PVdF-HFP. Both the mixtures were stirred thoroughly at room temperature for  $\sim 24\ \text{h}$  until the homogeneous mixture appeared. The ratio of EMPTFSI/SN (or LiTFSI/EMPTFSI/SN):PVdF-HFP was maintained to 4:1 (w/w). These mixtures were cast over glass petri-dishes, and acetone was allowed to evaporate slowly. Finally, the free-standing GPE films of thickness (0.70–0.80 mm) were obtained and stored in dry atmosphere to avoid moisture adsorption. The compositions of the GPEs are expressed in the text as:

- GPE-1: 5 mole% EMPTFSI in SN/PVdF-HFP
- GPE-2: 1 M LiTFSI in EMPTFSI/SN/PVdF-HFP

## 2.3. Characterization of ACs and GPEs

Morphology of the activated carbon powders was recorded

using field emission scanning electron microscope (FESEM, JEOL, JSM 5600). Gold was sputtered on the samples at low vacuum to obtain conducting surfaces, necessary to record FESEM images. XRD patterns of the activated carbons were obtained in the Bragg's angle ( $2\theta$ ) range from  $10^\circ$  to  $70^\circ$  using a high-resolution X-ray diffractometer (Model-D8 Discover, Bruker, USA) having  $\text{CuK}\alpha$  radiation of  $\lambda = 1.5406\ \text{\AA}$  (0.15,406 nm). Raman spectroscopic measurements were performed using a Renishaw-Invia Raman microscope (equipped with a charge-coupled device (CCD) detector) in a right-angle scattering geometry. Ar-ion laser of wavelength 514.5 nm and diameter  $1\text{--}2\ \mu\text{m}$  was used to excite the samples. The samples were kept in air during Raman measurements. Measurements of Brunauer, Emmett, and Teller (BET) surface area and other porosity parameters of the activated carbons were performed using a surface area and pore size analyzer (model: Gemini-V, Micromeritics, Norcross, USA).

The GPE films were characterized by measuring ionic conductivity and electrochemical stability window (ESW). The ionic conductivity of GPE films was evaluated by EIS in the frequency range from 1 Hz to 100 kHz at the cell SS|GPE|SS (SS being stainless steel foils). Temperature dependence of ionic conductivity were recorded on a Broadband Dielectric/Impedance Analyzer (Novocontrol C50 Alpha A, Germany) for the temperature range from  $-50$  to  $100^\circ\text{C}$ . ESW was estimated by linear sweep voltammetry (LSV). The EIS and ESW measurements were performed using an electrochemical analyzer (660 E, CH Instruments, USA).

## 2.4. Fabrication and characterization of EDLCs

EDLC cells were fabricated by spin coating the acetone solution of the gel polymer electrolyte over the surface of AC-electrodes, and the acetone was completely evaporated. Two such systems were placed over each other and pressed slightly to form plane geometry of the symmetric configuration of the cells. Following two configurations of EDLC cells using two different GPEs (GPE-1 and GPE-2) were under investigation:

- Cell-1: C|AC|GPE-1|AC|C
- Cell-2: C|AC|GPE-2|AC|C
- (C: flexible graphite sheet)

The performance the EDLCs was evaluated using EIS, CV and GCD tests. The EIS studies were performed in the frequency range from 10 mHz to 100 kHz using the electrochemical analyzer mentioned above. The CV responses were also recorded with the same electrochemical analyzer. The GCD tests were performed



using a software-controlled charge-discharge unit (BT-2000, Arbin Instruments, USA).

### 3. Results and discussion

#### 3.1. Characterization of ACs: morphological, structural and porosity analyses

Comparative morphological/structural studies and porosity analyses have been carried out on activated carbon powders, prepared by taking different ratios of starting biomass material, pinecone powder (PP) and activating agent ( $\text{ZnCl}_2$ ). The ratios of PP and  $\text{ZnCl}_2$  were taken to be 1:1, 1:2, 1:3 and 1:5 (w/w) and their codes are referred to as PP-Zn-1, PP-Zn-2, PP-Zn-3 and PP-Zn-5, respectively, in the text. Fig. 2a–c shows FESEM images of AC powders, prepared from different ratios of PP and  $\text{ZnCl}_2$ . Morphological texture of AC-powders has been found to vary significantly, when pinecone powder has been carbonized and activated with increasing content of  $\text{ZnCl}_2$ . In the case of low amount of activating agent (i.e., ratio of PP and  $\text{ZnCl}_2$ , 1:1 w/w), the resulting carbon material (PP-Zn-1) appears to be partially activated. The small spherical particles of carbon are densely interconnected, forming almost flat and compact surface, over which agglomerations of carbon particles of varying sizes are distributed haphazardly (Fig. 2a). These agglomerations appear to be activated carbons. On increasing the content of activating agent substantially (i.e., for the 1:3 w/w ratio of PP and  $\text{ZnCl}_2$ ), the sample (PP-Zn-3) shows bigger sized (10–30 nm) interconnected spherical carbon particles, which are almost

homogeneously distributed as compared to PP-Zn-1 sample (Fig. 2a and b). On further increasing the activating agent  $\text{ZnCl}_2$  i.e., the ratio of PP and  $\text{ZnCl}_2$ , (1:5 w/w), the resulting AC sample (PP-Zn-5) also shows 3D-interconnecting bigger sized spherical carbon particles, however, the texture of the material shows wide pores of varying sizes, mostly macropores ( $>50$  nm) (Fig. 2c).

Fig. 2d shows the comparative XRD patterns of the activated carbons derived from different weight ratios of pinecone powder and activating agent  $\text{ZnCl}_2$ . Two broad peaks between  $2\theta = 15^\circ$  to  $35^\circ$  and  $37^\circ$  to  $49^\circ$ , corresponding to (002) and (100) planes of carbon structure, respectively, appear in all the AC-samples. The broad peaks of (002) and (100) reflections indicate the highly amorphous/disordered nature of the activated carbons. One additional broad but weak peak has been noted between  $51^\circ$  and  $57^\circ$  for the AC sample PP-Zn-1, activated with low concentration of  $\text{ZnCl}_2$ , is assigned to (004) plane [78]. This peak disappears for the AC-samples, activated using higher amount of  $\text{ZnCl}_2$  (2, 3 and 5 wt%), indicating the disruption of residual graphite-like layer in the carbon material.

Fig. 3 shows Raman spectra of all the AC-powders. The D-bands, corresponding to defects/disorder, and G-bands, which are related to graphitic structure of carbon, are observed for all the AC powders under investigation (PP-Zn-1 to PP-Zn-5). The presence of D and G-bands with significant intensities indicate the existence of the substantial amount of defects/disorder at microscopic level along with the haphazardly distributed graphitic layers in all the AC samples under the present investigation. The ratio of areal intensities corresponding to these signature D and G-bands ( $I_D/I_G$ )

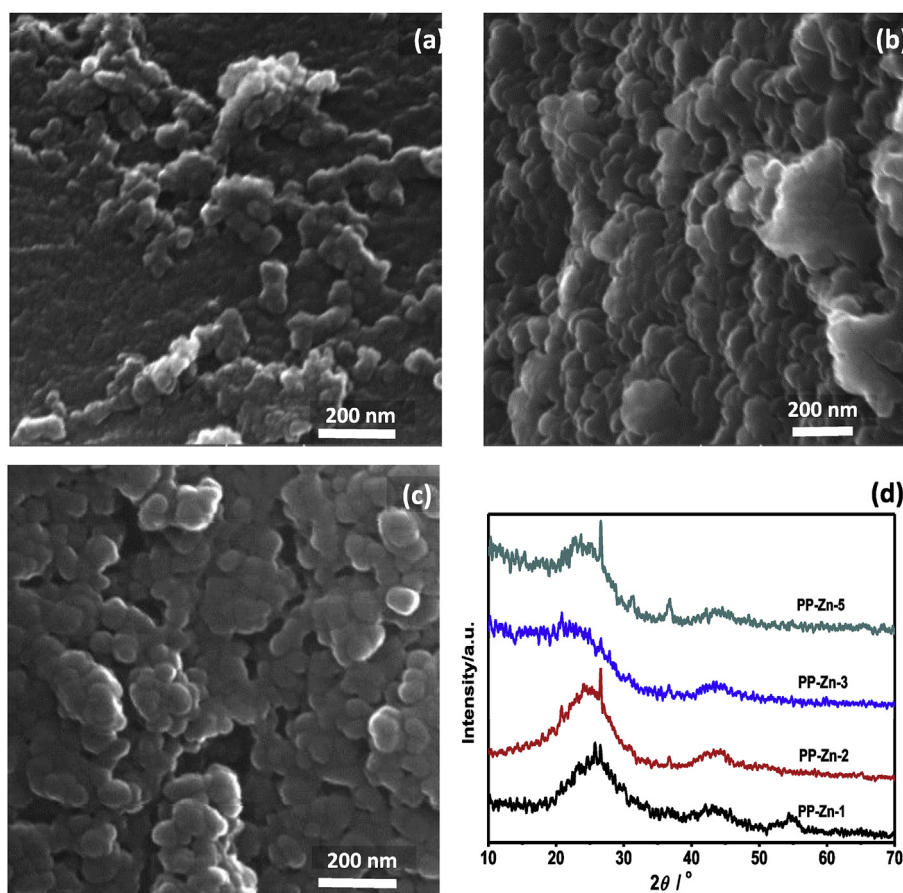


**Fig. 2.** FESEM images of activated carbons, prepared from different weight ratios of pinecone powder (PP) and activating agent  $\text{ZnCl}_2$ ; (a) 1:1 w/w (PP-Zn-1), (b) 1:3 w/w (PP-Zn-3), and (c) 1:5 w/w (PP-Zn-5). Fig. (d) shows XRD patterns of different AC-powders.

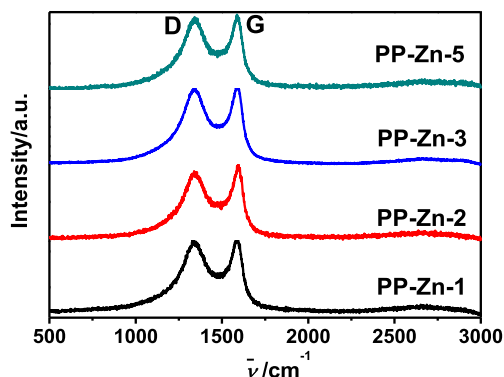


Fig. 3. Raman spectra of AC powders, produced from different ratio of pinecone powder (PP) and activating agent  $\text{ZnCl}_2$ .

has been estimated for each AC sample after de-convoluting these peaks (Table S1). The de-convoluted peaks are shown in Fig. S1 for each AC sample. The areal intensity ratios ( $I_D/I_G$ ) are found to be almost same (ranging from 2.66 to 2.98) for all the samples. This indicates that the amount of microscopic defects/disorder is almost same for all the AC samples, produced taking different amount of activating agent  $\text{ZnCl}_2$ .

Fig. 4(a and b) shows  $\text{N}_2$ -adsorption-desorption isotherms and pore size distribution of the pinecone-derived activated carbons. A sudden initial increase in isotherms, indicating major uptake of nitrogen, has been observed for each AC samples at low relative pressure i.e.,  $P/P_0 < 0.005$ . The activated carbon PP-Zn-1, prepared employing low amount of  $\text{ZnCl}_2$ , shows Type-I isotherm (according to IUPAC classification), i.e. a sudden initial jump in  $\text{N}_2$ -adsorption followed by a perfect saturation with respect to  $P/P_0$  [74]. On increasing the content of  $\text{ZnCl}_2$  by two times (i.e., PP: $\text{ZnCl}_2$  ratio 1:2 w/w), the resulting activated carbon (PP-Zn-2) tends towards Type-IV isotherm. In this case, there is rapid gas adsorption initially up to  $P/P_0 \sim 0.005$ , followed by a gradual increase in adsorption up to  $P/P_0 \sim 0.5$ , beyond that it gets saturated as in the case of Type-I isotherms. The material shows a small hysteresis also while desorption. These features indicate predominant microporosity in AC powder (PP-Zn-2) along with small proportion of mesoporous interiors. On employing weight of activating agent  $\text{ZnCl}_2$  three times with respect to pinecone powder (i.e. for PP: $\text{ZnCl}_2$  ratio 1:3 w/w), the AC powder PP-Zn-3 shows Type-IV isotherm of  $\text{N}_2$ -adsorption with prominent H4-type hysteresis while desorption. After a sudden jump up to  $P/P_0 \sim 0.005$ , the isotherm shows gradual increase in  $\text{N}_2$ -adsorption for the entire  $P/P_0$  range (Fig. 4a). It may be noted that the initial increase in adsorption up to  $P/P_0 \sim 0.005$  and the gradual increase beyond that is observed to be the highest among all the AC powders. These features indicate the highest

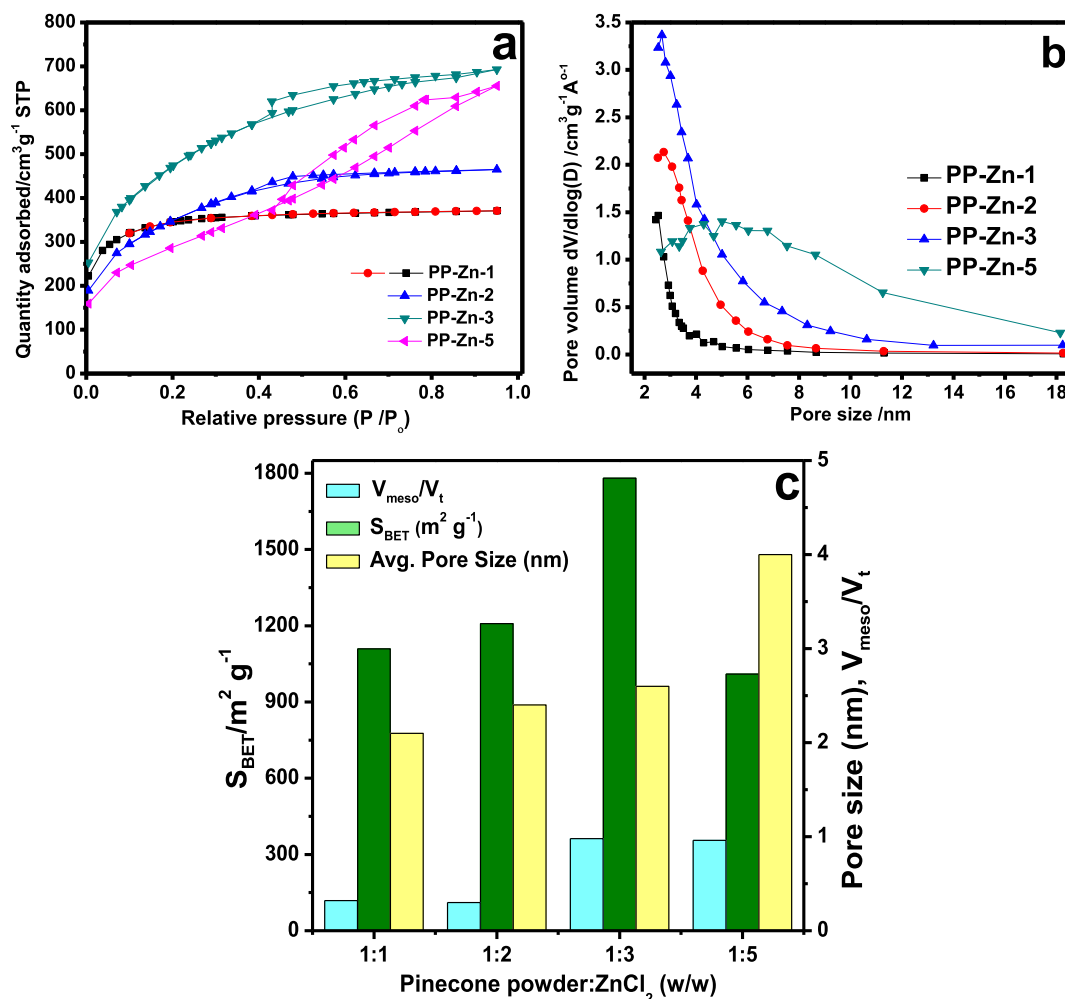


Fig. 4. (a)  $\text{N}_2$ -adsorption-desorption isotherms, and (b) pore size distribution of AC-powders, produced from different proportions of biomass material pinecone powder (PP) and activating agent  $\text{ZnCl}_2$ . Fig. (c) shows the bar diagram indicating the variation of BET specific surface area, mesoporous volume with respect to total volume and average pore size as function of activating agent  $\text{ZnCl}_2$ .

microporosity in AC powder PP-Zn-3 along with large proportion of mesoporous character.

On further increase in  $\text{ZnCl}_2$  content, i.e., for PP: $\text{ZnCl}_2$  ratio 1:5 w/w, the activated carbon (PP-Zn-5) shows Type-IV isotherm with H2-type hysteresis while desorption [74]. The pattern of isotherm is different from that of the AC powder PP-Zn-3 (Fig. 4a). After a sudden increase up to  $P/P_0 \sim 0.005$ , the isotherm follows a slow increase in adsorption up to  $P/P_0 \sim 0.55$  and beyond that, it shows a faster increase up to the saturation point ( $P/P_0 \sim 0.95$ ). These patterns along with hysteresis indicate the co-existence of micro- and mesoporosity in the material (PP-Zn-5). The increasing pattern with higher slope beyond  $P/P_0 \sim 0.55$  and the nature of hysteresis during desorption indicate the existence of substantial proportion of mesopore interiors in the material having larger pore sizes. The presence of macropores ( $>50$  nm) in this AC-powder is also indicated in FESEM image (Fig. 2c), discussed above.

Fig. 4b depicts the pore size distribution of the AC powders, calculated using the Barret-Joyner-Halenda (BJH) method [74]. It has been observed that the AC powders prepared from 1:1, 1:2 and 1:3 weight ratios of PP: $\text{ZnCl}_2$  show highest concentration of mesopores of size at 2.5–3 nm. The pore-size distribution has been found to increase for wider ranges up to  $\sim 11$  nm with increasing content of  $\text{ZnCl}_2$  to activate the carbon powder up to 1:3 weight ratio of PP: $\text{ZnCl}_2$ . On increasing the  $\text{ZnCl}_2$  content further, i.e. for PP: $\text{ZnCl}_2$  of 1:5 w/w, the material shows a peculiar broad

distribution of pore sizes in the mesoporous range and total pore volume decreases significantly (Fig. 4b and Table S2). This indicates that the larger pores created due to larger amount of  $\text{ZnCl}_2$  collapse partially and blocked.

A bar diagram (Fig. 4c) represents the variation of BET surface area, average pore size and mesopore volume to total pore volume ratio of AC powders as a function of activating agent  $\text{ZnCl}_2$ . Detailed quantitative values of surface area and porosity parameters are given in Table S2. The total pore volume has been estimated at the pressure  $P/P_0 \sim 0.95$ . The mesoporous volume has been calculated by subtracting the micropore volume from the total pore volume (Table S2). The presence of combined micro- and meso-pores in the AC electrodes, in appropriate proportion, provides the enhanced performance of EDLCs. The AC powder, prepared from the mixture of PP: $\text{ZnCl}_2$  in the ratio of 1:3 w/w, shows optimum parameters with highest specific surface area and sufficient mesoporosity (Fig. 4c and Table S2). Thus, the AC material PP-Zn-3 has been found suitable as EDLC electrodes.

### 3.2. Properties of GPEs

The gel polymer electrolytes GPE-1 (PVdF-HFP/SN/EMPTFSI) and GPE-2 (PVdF-HFP/SN/EMPTFSI/LiTFSI) are in the form of semi-transparent, mechanically/dimensionally stable and flexible thick films. A photograph of the typical film of GPE-2 is shown in Fig. 5a,

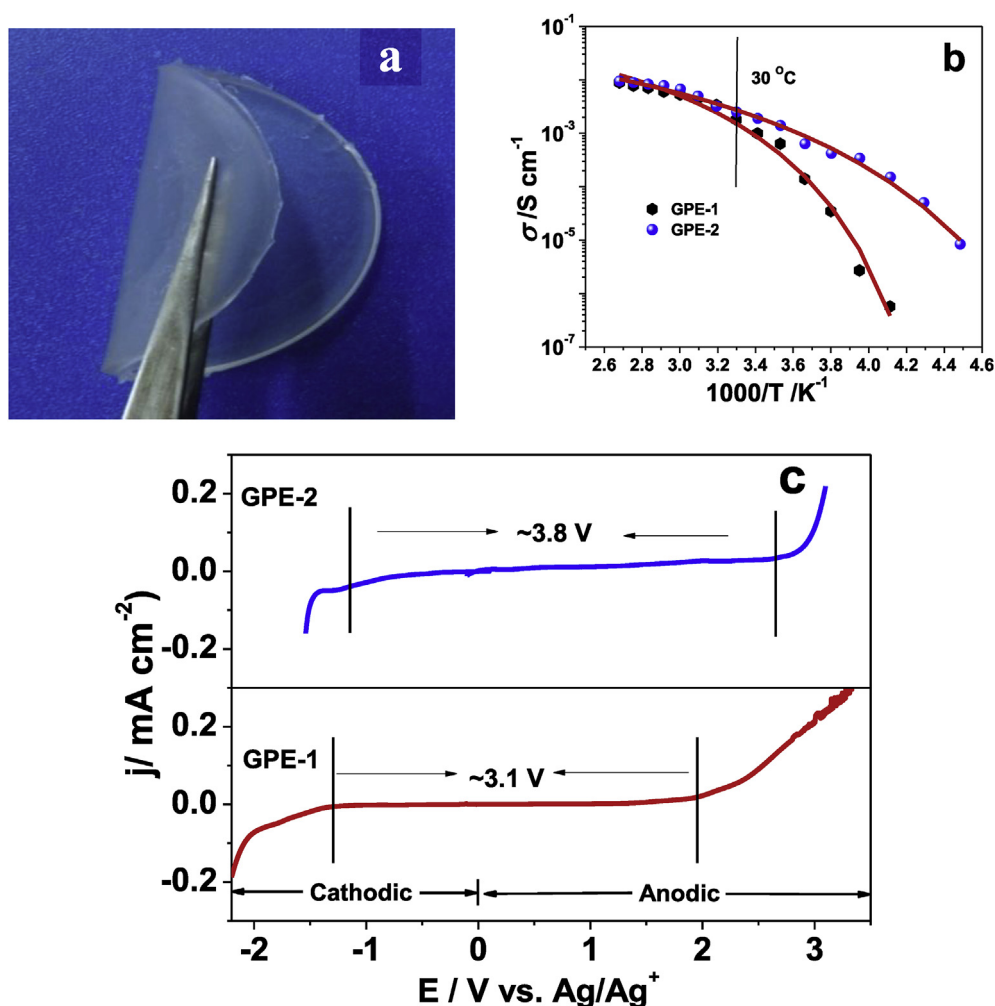


**Fig. 5.** (a) An image of gel polymer electrolyte PVdF-HFP/SN/EMPTFSI/LiTFSI (GPE-2) film, indicating its flexible nature, (b) temperature dependent ionic conductivity profiles of GPEs, PVdF-HFP/SN/EMPTFSI (GPE-1) and PVdF-HFP/SN/EMPTFSI/LiTFSI (GPE-2), and (c) LSV plots, indicating electrochemical stability window of the electrolytes GPE-1 and GPE-2.

indicating its flexible nature. Photographs of the films, subjected to other deforming stresses namely: multiple folding, twisting and stretching are shown in Fig. S2. These confirm the flexible nature and resilience of the GPE films against these stresses. The temperature dependent ionic conductivity profiles i.e.,  $\sigma$  versus  $1/T$  plots of GPE-1 (without Li-salt) and GPE-2 (with Li-salt) are shown in Fig. 5b. Both the profiles show the curved nature of variation, which can be fitted well with Vogel–Tammann–Fulcher (VTF) equation, expressed as:

$$\sigma = AT^{-1/2} \exp\left(\frac{-B}{T - T_0}\right) \quad (1)$$

where  $A$  is pre-exponential factor, referred to the conductivity at infinitely high temperature,  $B$  is pseudo-activation energy related with the critical free-volume for ionic conduction, and  $T_0$  equilibrium glass transition temperature. The fitting parameters  $A$ ,  $B$  and  $T_0$  have been evaluated using non-linear least square (NLLS) fitting of these plots and given in Table S3. Fragility index ( $F$ ) of the GPEs has been estimated from the expression:  $F = T_0/B$  (Table S3), which is inversely related to the strength of the materials [12]. It may be noted that on the addition of LiTFSI in the composition PVdF-HFP/SN/EMPTFSI, the strength of the GPE (GPE-2) improves slightly. The mechanical/dimensional stability of GPE-2 is found to be high enough (Fig. S2) to be used as electrolyte in supercapacitors.

The electrical conductivity of PVdF-HFP/SN (weight ratio 20:80) is reported to be  $\sim 2.2 \times 10^{-7} \text{ S cm}^{-1}$ , primarily due to possible impurities [67]. On adding 5 mole% OIPC (EMPTFSI), the conductivity of GPE PVdF-HFP/SN/EMPTFSI (GPE-1) increases to  $\sim 1.53 \times 10^{-3} \text{ S cm}^{-1}$  at room temperature ( $30^\circ\text{C}$ ). In this composition, the non-ionic plastic crystal SN plays a dual role of: (i) high dielectric constant medium to dissociate OIPC (EMPTFSI) in its component ions for ionic conductivity, and (ii) as rotator to support ionic mobility of the component ions ( $\text{EMP}^+$  and  $\text{TFSI}^-$ ) [67]. On further addition of Li-salt (LiTFSI), ionic conductivity of the GPE (GPE-2) has been enhanced to  $\sim 2.87 \times 10^{-3} \text{ S cm}^{-1}$  at room temperature ( $\sim 30^\circ\text{C}$ ). This indicates that the Li-ion mobility in the plastic crystalline medium is higher than the component ions of OIPC. The mechanically flexible nature and high ionic conductivity of the GPEs (GPE-1 and GPE-2) indicate their suitability as separator/electrolyte to fabricate solid-state EDLCs.

The electrochemical stability window (ESW) is important characteristic of an electrolyte, which determines the maximum operating voltage limit of the electrochemical devices like batteries/supercapacitors. The ESW of the GPE-1 and GPE-2 has been estimated by LSV (Fig. 5c), recorded on the cell: SS|GPE|Ag; where SS is stainless steel sheet, working as blocking electrode and Ag represents silver foil, used as reversible electrode. In LSV measurements, the SS-sheet was employed as working electrode, whereas Ag-foil acted as combined counter and reference electrodes. The ESW of the GPE-1 film (without LiTFSI) has been found to be  $\sim 3.1 \text{ V}$  versus  $\text{Ag}/\text{Ag}^+$ . On incorporating Li-salt in the GPE composition, the GPE-2 film offers an improvement in ESW to  $\sim 3.8 \text{ V}$  versus  $\text{Ag}/\text{Ag}^+$  (Fig. 5c). It may be noted that the electrochemical stability window is approximately same in the cathodic region for both the electrolytes, while it is slightly higher in the anodic region from 1.95 to 2.65 V on the addition of Li-salt (Fig. 5c). This indicates that the Li-ions in GPE-2 show better stability on the Ag-electrode as compared to that of  $\text{EMP}^+$  ions of GPE-1 (without Li-salt). It is well established that the ESW of electrolytes, observed to be  $> 3 \text{ V}$ , is wide enough for the EDLC/supercapacitor applications.

### 3.3. Characteristics of EDLC cells

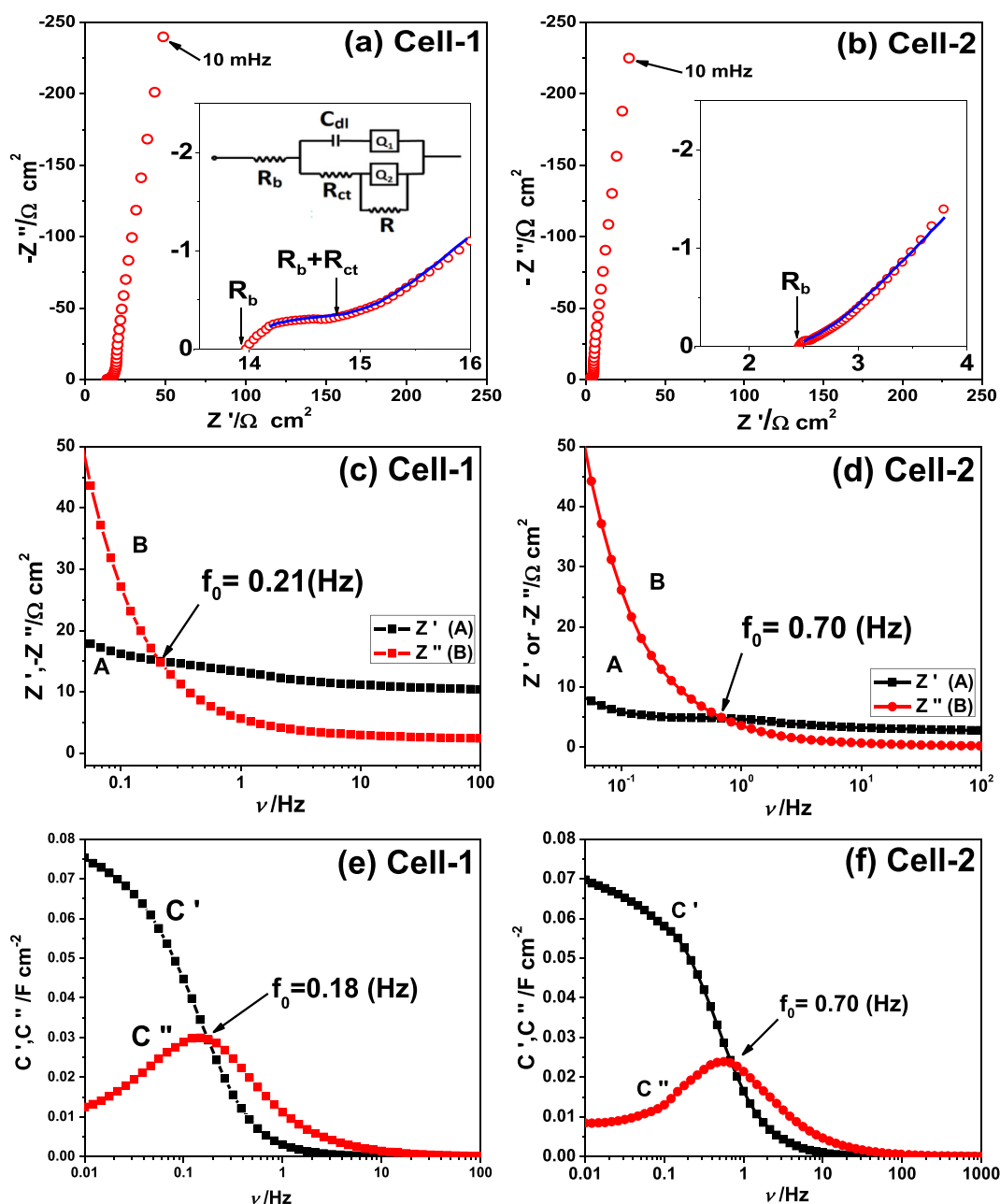
#### 3.3.1. EIS

Fig. 6(a and b) represents the EIS (i.e.,  $Z''$  vs.  $Z'$ ) plots, also referred to as Nyquist plots, of the EDLCs (Cell-1 and Cell-2), respectively, in the frequency range from 10 mHz to 100 kHz. The patterns of the EIS plots of both the cells have been found to be capacitive i.e., the dispersion curves of  $Z''$  with respect to  $Z'$  vary almost parallel to  $Z''$ -axis in the low frequency region. The dispersion curves (almost semi-circular spur followed by linear pattern) in the high frequency region (Fig. 6a and b, insets) show different characteristics of the cells, particularly, the bulk resistance of electrolyte and nature of the electrode-electrolyte interfaces. The intercepts of the curves with  $Z'$ -axis (as indicated by arrows) in the high frequency region represent the bulk resistance ( $R_b$ ), which is owing to the resistance of electrolytes and charge-transfer resistance ( $R_{ct}$ ). The charge-transfer resistance is associated with the possible fast faradaic reaction(s) due to the presence of surface functionalities adsorbed on the activated carbon electrodes. The presence of surface functionalities on activated carbon has been discussed in the following section. In the middle frequency region, both the cells show the linear pattern of impedance variation making  $\sim 45^\circ$  angle with the  $Z'$ -axis (Fig. 6a and b). This linear variation is attributed to Warburg impedance region, which is mainly related to the diffusion of electrolyte ions and the porous character of the electrodes. The specific capacitance of the EDLCs have been evaluated at low frequency, particularly, at 10 mHz in the present studies. The expression  $C = 1/\omega Z''$  (where  $\omega$  is angular frequency) was used to evaluate the overall capacitance of each cell at 10 mHz. The specific capacitance ( $C_s$ ) was evaluated by:  $C_s = 2C/m$ , where  $m$  is the mass of the AC material employed in single electrode. The values  $R_b$ ,  $R_{ct}$  and  $C_s$  have been evaluated and presented in Table 1. Suitability of the capacitive combination of porous AC electrodes with flexible gel polymer electrolytes (GPE-1 and GPE-2) has been indicated by the high values of specific capacitance ( $184\text{--}202 \text{ F g}^{-1}$ ) of the capacitor cells (Table 1).

The impedance data of high and mid-frequency regions for both the cells have been fitted with modified Randles circuit, as depicted in the inset of Fig. 6a. The semi-circular arc is represented by a parallel combination of charge transfer resistance ( $R_{ct}$ ) and capacitance ( $C_{dl}$ ), in series with bulk resistance of the electrolyte ( $R_b$ ). The impedance plot could be fitted well with two constant phase elements ( $Q_1$  and  $Q_2$ ) and a faradaic resistance  $R$  parallel to  $Q_2$ . The fitting parameters are given in Table S4 for both the cells (Cell-1 and Cell-2). The fitted data, particularly,  $R_b$  and  $R_{ct}$  values almost match with experimental values (Table 1), which indicates that the model used for fitting the impedance data was correct.

A comparison of the values of  $R_b$ ,  $R_{ct}$  and  $C_s$  indicates the effective role of the electrolytes, GPE-1 and GPE-2, on the performance of Cell-1 and Cell-2. It may be noted that the specific capacitance of Cell-2 (with Li-salt containing electrolyte, GPE-2) offers a slight enhancement only with respect to that of Cell-1 (with electrolyte GPE-1 without Li-salt, containing OIPC/SN only). This indicates that component ions of IL are replaced by  $\text{Li}^+$  ions in the pores of AC electrodes to form double layers. Also, few small size pores, which were not accessible to relatively bigger size component ions of IL, have also been accommodated by  $\text{Li}^+$  ions, forming additional double layers. Further, the EDLC cell (Cell-2) offers substantial lowering in bulk resistance ( $R_b$ ) and charge-transfer resistance ( $R_{ct}$ ) as compared to that for Cell-1. This indicates the significant role of  $\text{Li}^+$  ion incorporated GPE (GPE-2), employed as electrolyte in Cell-2. It confirms that the movement of  $\text{Li}^+$  ions through the pores of activated carbon electrodes are facile





**Fig. 6.** (a and b) EIS plots of EDLC cells, insets represent expanded high frequency regions, (c and d) real and imaginary impedances  $Z'$  and  $Z''$  versus frequency i.e., Bode plots of the cells, and (e and f) real and imaginary capacitance variation as function of frequency of the cells.

**Table 1**

Various parameters of EDLC cells, evaluated from EIS analysis.

Capacitor Cells	$R_b(\Omega \text{ cm}^2)$	$R_{ct}(\Omega \text{ cm}^2)$	$C_s(\text{F g}^{-1})$	Response freq. $f_0(\text{Hz})$	Response time $\tau_0(\text{s})$	Energy $E_0$ at $f_0(\text{Wh kg}^{-1})$	Pulse power $P_0(\text{kW kg}^{-1})$
Cell-1	14.1	1.09	184–192	0.20	5.0	11.0	8.4
Cell-2	2.4	0.18	191–202	0.70	1.4	11.4	28.6

as compared to the component ions of IL in the electrode-electrolyte interfacial region.

Incorporation of  $\text{Li}^+$  ions in the GPE, employed as separator/electrolyte, has also influenced substantially the rate capability of the EDLC cells, studied adopting Miller's approach [79]. Accordingly, Bode plots (i.e., the variation of  $Z'$  and  $Z''$  against frequency) have been recorded for both the cells (Fig. 6c and d). The resonant

frequency ( $f_0$ ) for each cell has been noted from the point at which the two plots intersect each other at phase angle of  $45^\circ$ , as indicated by arrow in Fig. 6(c and d). The response time  $\tau_0$ , which is the characteristic of a capacitor cell and determine the rate capability, is reciprocal of  $f_0$ . An important parameter, referred to as pulse power density,  $P_0$  (also called 'Fig. of merit') has been evaluated for each EDLC cell from the equation:  $P_0 = E_0/\tau_0$ , where  $E_0$  is the specific



energy, evaluated at the frequency  $f_0$ . The value of  $E_0$  has been evaluated from the expression:  $E_0 = \frac{1}{2}C_{s0}V^2$  for each cell, where  $C_{s0}$  is the specific capacitance at  $f_0$  and  $V$  is the maximum voltage of the EDLC cell i.e., 1.5 V in the present case. The values of  $f_0$ ,  $\tau_0$ ,  $E_0$  and  $P_0$  are given in Table 1 for both the cells. From the Taberna approach [80] also, in which real and imaginary capacitances ( $C'$  and  $C''$ ) are plotted against frequency, the values of  $f_0$  for both the cells (as shown by arrows in Fig. 6e and f) are observed to be the same or very close to the values from Miller's approach. The variations of  $C'$  and  $C''$  versus frequency are found to be typical of the EDLCs [80].

We can observe the substantial (~3.5 times) increase in the resonant frequency  $f_0$  (hence, lowering in response time  $\tau_0$ ) from Cell-1 to Cell-2, when electrolyte GPE-1 (without Li-salt) is replaced by Li-salt containing electrolyte GPE-2. Accordingly, the pulse power density  $P_0$  increases with almost same proportion, as the specific energy  $E_0$  values are almost same for both the cells. This reveals the substantial enhancement of rate capability of the EDLC cell (Cell-2), which employs the electrolyte GPE-2 containing Li-salt. High ionic conductivity of GPE-2 and facile movement of  $\text{Li}^+$  ions through the micro- and mesoporous interiors of AC electrodes offer synergistic effect to obtain higher rate performance of Cell-2 with respect to Cell-1.

### 3.3.2. CV

The electrochemical behavior of the EDLC cells has been tested by CV measurements carried out in two electrodes arrangements (Fig. 7). Fig. 7a shows the CV patterns of a typical cell (Cell-2, comprising Li-salt containing GPE), recorded with gradually increasing voltage ranges up to 2 V at a scan rate of  $10 \text{ mV s}^{-1}$  at room temperature. This indicates that the EDLC cells can be cycled

well in the voltage range of 0–2 V. Comparative CV patterns (Fig. 7b) shows higher voltammetric current (hence higher specific capacitance) for Cell-2 (with GPE containing Li-salt) with respect to that of the Cell-1 (with GPE without Li-salt). This shows the superior performance of Cell-2 and direct effect of Li-ions on the capacitive performance at the interfaces of the EDLC.

Fig. 7c shows the scan rate dependent voltammograms of a typical EDLC cell (Cell-2). The CV patterns of Cell-1 for different scan rates are shown in Fig. S3 for a reference. Almost rectangular shapes and mirror image like CV patterns below and above the zero-current line, indicating EDLC like behavior of Cell-2, have been observed for different scan rates up to  $300 \text{ mV s}^{-1}$ . This indicates moderately high rate capability of the Cell-2 owing to facile transport of  $\text{Li}^+$  ions through porous interiors of AC electrodes. The same result regarding rate capability has been observed in terms of response time in impedance analysis as discussed above. Fig. 7d depicts the variations of specific capacitance ( $C_s$ ), evaluated from CV patterns, with respect to scan rates for both the cells (Cell-1 and Cell-2). The values of  $C_s$  have been evaluated from the expression:  $C_s = \frac{2 \times i}{m \times s}$ , where  $i$  is voltammetric current,  $s$  is scan rate and  $m$  is mass of AC material, used in single electrode. It can be noted that a gradual decrease in specific capacitance has been observed with respect to scan rates for both the cells (Cell-1 and Cell-2), however, the Cell-2 shows higher specific capacitance compared to Cell-1 at each scan rate up to  $300 \text{ mV s}^{-1}$ . This shows the better performance of  $\text{Li}^+$  ions over the other electrolyte ions (component ions of IL) in proper double layer formation and easy ion transport through pores of AC electrodes, as mentioned above.

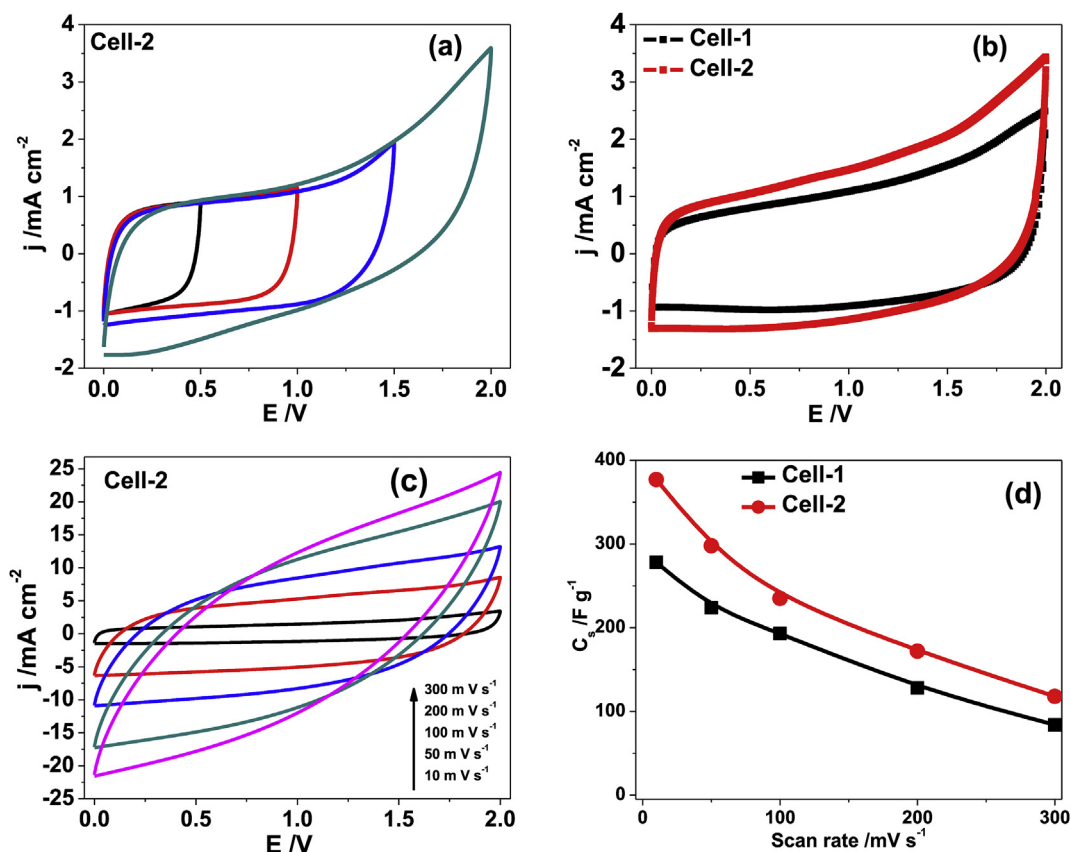


Fig. 7. (a) CV patterns of Cell-2 for gradually increasing voltage ranges, recorded at a scan rate of  $10 \text{ mV s}^{-1}$ , (b) comparative CV patterns of Cell-1 and Cell-2, at scan rate  $10 \text{ mV s}^{-1}$ , (c) CV patterns of typical cell (Cell-2) at different scan rates, and (d) scan rate dependence of specific capacitance for Cell-1 and Cell-2.

### 3.3.3. Charge-discharge

In order to ascertain maximum operating voltage limit of the EDLCs, a typical cell (Cell-2) has been charged and discharged for varying voltage limit from 0 to 2 V at current density of  $1 \text{ mA cm}^{-2}$  ( $\sim 1.4 \text{ A g}^{-1}$ ) as depicted in Fig. 8a. It has been noted that the charging characteristic becomes more deviated from linear pattern beyond 1.5 V. Hence, the charge-discharge studies of the EDLC cells have been performed up to 1.5 V in the present studies. It is worth noting that although the ESW of the GPEs, employed in the present EDLCs, is more than 3 V (discussed earlier), the charging voltage of the devices is limited to  $\sim 1.5 \text{ V}$  only. The most possible reason is the presence of surface functionalities (carbonyl, carboxyl, hydroxyl,

phenols, etc.) with the porous carbon electrodes [81–83], which possibly react with different components of GPEs and restrain the potential window [81]. The presence of functional groups has been confirmed from FTIR spectrum of the activated carbon as depicted in Fig. S4.

Fig. 8b illustrates the GCD patterns of the typical cell (Cell-2), recorded at different constant currents. The charge-discharge characteristics of Cell-1 at different current densities are also given in Fig. S5, for comparison. Both the cells show the patterns comprising initial sudden drop in  $V-t$  profiles followed by linear variations, indicating characteristics of real EDLCs. The initial drops are owing to the ohmic drop across the equivalent series resistance

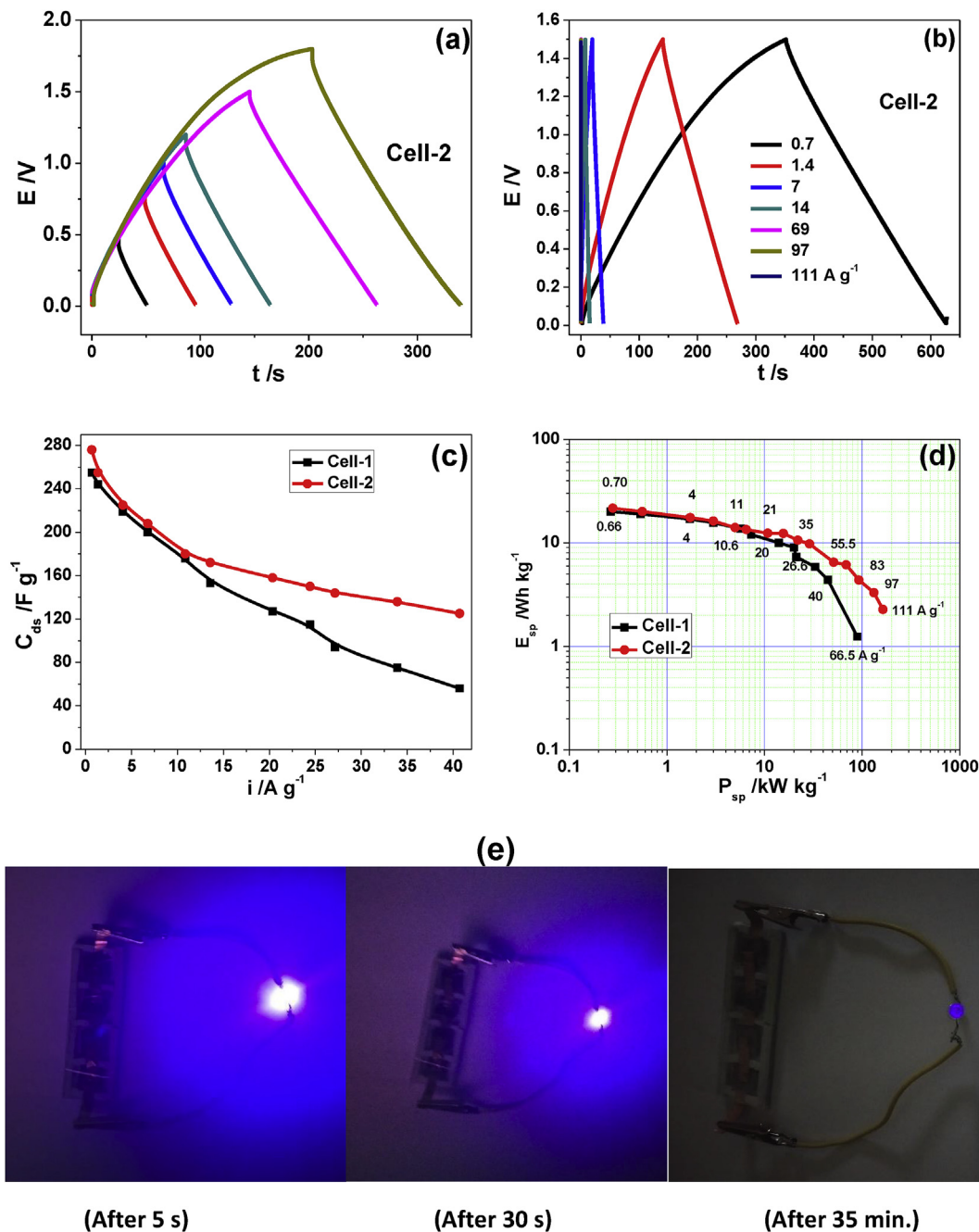


**Fig. 8.** (a) Charge-discharge curves for Cell-2 (with Li-salt containing GPE) for varying voltage limits recorded at constant current of  $1.0 \text{ mA cm}^{-2}$  ( $1.4 \text{ A g}^{-1}$ ), (b) charge-discharge curves for the typical Cell-2 at different current densities, (c) variation of discharge capacitance of the EDLC cells as a function of current density, and (d) Ragone plots of the cells; numbers marked on the curves represent discharge currents in  $\text{A g}^{-1}$ , and (e) demonstration of the LED glow powered by EDLC cells, at different time intervals.

**Table 2**Typical charge–discharge characteristics of EDLC cells, evaluated at a constant current  $1 \text{ mA cm}^{-2}$  ( $1.3\text{--}1.4 \text{ A g}^{-1}$ ).

EDLC Cells	ESR( $\Omega \text{ cm}^2$ )	Specific discharge capacitance ( $C_{ds}$ ) ( $\text{F g}^{-1}$ )	Specific energy ( $E$ )( $\text{Wh kg}^{-1}$ )	Max. specific power ( $P_{\text{max}}$ )( $\text{kW kg}^{-1}$ )
Cell-1	9.7	244	19	39.3
Cell-2	7.0	255	20	55.7

(ESR), whereas, the linear variation characterizes capacitive nature of the cells. The values of ESR have been evaluated by:  $\text{ESR} = \Delta V / (2 \times I)$ , where  $\Delta V$  is voltage drop and  $I$  is constant current. The discharge specific capacitance ( $C_{ds}$ ) values are evaluated from:  $C_{ds} = \frac{2I \times \Delta t}{m \times \Delta V}$ , where  $\Delta V / \Delta t$  is the slope of linear portion of discharge curve and  $m$  is mass of the activated carbon incorporated in single electrode. The values of ESR and  $C_{ds}$  of the EDLCs (Cell-1 and Cell-2), evaluated at a typical current density of  $1 \text{ mA cm}^{-2}$  (i.e.,  $1.3\text{--}1.4 \text{ A g}^{-1}$ ), are listed in Table 2. These values are observed to be almost comparable to the cell resistance ( $R_b$ ) and specific capacitance ( $C_s$ ), evaluated from EIS analyses, discussed above (Table 1). Further, it may be specifically noted that specific capacitance ( $255 \text{ F g}^{-1}$ ) of Cell-2 is high. However, the value is comparable to the specific capacitance reported for many EDLCs fabricated with carbon electrodes derived from different biomasses/bio-wastes and liquid/gel polymer electrolytes (Table 3). The possible reason to observe high specific capacitance is the hierarchical porosity in the present activated carbon containing mixed micro- and mesoporous interiors, discussed above. In such cases, mesopores increase the accessibility of electrolyte ions to a larger number of micropores and act as reservoir of electrolyte ions [3]. So, apart from specific surface area of activated carbon, the appropriate ratio of meso- to micro-porosity is an important factor to obtain higher specific

capacitance.

Specific energy ( $E$ ) of the devices has been evaluated from the expression:  $E = \frac{1}{2} C_{ds} V^2$ , where  $V$  is the rated voltage ( $1.5 \text{ V}$  in the present case). The maximum specific power ( $P_{\text{max}}$ ) has been estimated from:  $P_{\text{max}} = V^2 / (8m \times \text{ESR})$ , where  $m$  is the mass of AC material in single electrode. Typical values of  $E$  and  $P_{\text{max}}$ , evaluated for current density  $1.0 \text{ mA cm}^{-2}$  ( $1.3\text{--}1.4 \text{ A g}^{-1}$ ) are given in Table 2 for both the cells. A comparison shows that significant increase in specific energy has not been observed in Cell-2, in which the electrolyte GPE-1 (without Li-salt) is replaced by the  $\text{Li}^+$  incorporated electrolyte GPE-2. This is because of an insignificant increase in specific capacitance of the EDLC cell (Cell-2) compared to Cell-1 (Table 2). On the other hand, a significant improvement has been observed in specific power ( $P_{\text{max}}$ ) of the Cell-2 (employing  $\text{Li}^+$  ion containing GPE) as compared to Cell-1 with only plastic crystal containing GPE-1 (Table 2). This observation is directly associated with the higher ionic conductivity of the electrolyte GPE-2 and hence, substantial lowering in ESR of Cell-2 with respect to Cell-1 (Table 2). Table 3 compares the performance characteristics (e.g. specific capacitance, energy and power) of the present EDLCs (fabricated with pinecone-derived porous AC electrodes) with the devices configured with porous carbons produced from other biomasses/bio-wastes, reported in literature. It has been noticed

**Table 3**

Comparative characteristic parameters of symmetric EDLCs, fabricated using AC electrodes derived from different biomasses/bio-wastes.

Biomass/bio-waste materials	Acti-vating agent	Surface area ( $\text{m}^2 \text{ g}^{-1}$ )	Electrolyte used	Specific Capacitance $C_{sp}$ ( $\text{F g}^{-1}$ )	Specific energy $E$ ( $\text{Wh kg}^{-1}$ )	Specific power $P$ ( $\text{kW kg}^{-1}$ )	Ref.
Coffee shells	$\text{ZnCl}_2$	842	6 M KOH	156 ( $1 \text{ mV s}^{-1}$ )	.....	.....	[32]
Walnut shells	$\text{ZnCl}_2$	1197	6 M KOH	292 (80 mA)	7.3	0.77	[85]
Celtuce leaves	KOH	3404	2 M KOH	273 ( $0.5 \text{ A g}^{-1}$ )	.....	.....	[11]
Sunflower seed shells	KOH	1162	15 wt% KOH aqueous solution	244 ( $0.25 \text{ A g}^{-1}$ )	4.4	2.4	[33]
Cherry stones	KOH	1100, 1300	2 M $\text{H}_2\text{SO}_4$ , 1 M $(\text{C}_2\text{H}_5)_4\text{NBF}_4/\text{ACN}$	230, 120 ( $1\text{--}100 \text{ mA cm}^{-2}$ )	1.0, 4.0	1.5, 5.5	[34]
Potato starch	KOH	2342	6 M KOH	335 ( $50 \text{ mA g}^{-1}$ )	.....	.....	[35]
Corn grains	KOH	3420	6 M KOH	257 ( $50 \text{ mV s}^{-1}$ )	.....	.....	[86]
Brussel sprouts	KOH	2410	6 M KOH	255 ( $0.5 \text{ A g}^{-1}$ )	6.4	0.05	[87]
Waste coffee beans	$\text{ZnCl}_2$	1019	1 M $\text{H}_2\text{SO}_4$	368 ( $0.05 \text{ A g}^{-1}$ )	20	6	[83]
Pinecone	KOH	1515	1 M $\text{Na}_2\text{SO}_4$	137 ( $0.5 \text{ A g}^{-1}$ )	19	0.1	[52]
Pinecone	KOH	808	6 M KOH	277* ( $0.5 \text{ A g}^{-1}$ )	24.6*	0.4	[53]
Pinecone petals	KOH	3950	1 m LiPF 6 in ethylene carbonate/dimethyl carbonate (1:1 v/v, 1 m LiPF 6 in ethylene carbonate/dimethyl carbonate (1:1 v/v, 1 m LiPF 6 in 1 m LiPF 6 in 1 M LiPF6 in EC/DMC	142 ( $1 \text{ A g}^{-1}$ )	61	4.5	[51]
Coconut shell	$\text{ZnCl}_2$	2100	PVdF-HFP/ BMPTFSI/SN PVdF-HFP/EMITf/ SN	210–234 ( $1 \text{ mA cm}^{-2}$ ) 225–253 ( $1 \text{ mA cm}^{-2}$ )	33 35	7 12	[36] [36]
Almond shell	$\text{CaCl}_2$	214	PVdF-HFP/PC/ $\text{MgClO}_4$ /EDiMIM-BF <sub>4</sub>	452 ( $5 \text{ mA cm}^{-2}$ )	62.76	2.1	[37]
Pinecone	$\text{ZnCl}_2$	1781	PVdF-HFP/EMP-TFSI/SN  PVdF-HFP/EMP-TFSI/SN/LiTFSI	244 ( $1.4 \text{ A g}^{-1}$ )  255 ( $1.4 \text{ A g}^{-1}$ )	19  20	39.3  55.7	Present work Present work

\* Asymmetric configuration of capacitor with pinecone AC as anode and activated expanded graphite as cathode.

ACN: Acetonitrile; EC: ethylene carbonate; PC: Propylene carbonate; DMC: Dimethyl carbonate; PVdF-HFP: Poly(vinylidene fluoride-co-hexafluoropropylene); BMPTFSI: 1-butyl-1-methyl pyrrolidinium bis(trifluoro-methane sulfonyl) imide; EMITf: 1-ethyl-3-methyl imidazolium trifluoromethane sulfonate; EDiMIM-BF<sub>4</sub>: 1-ethyl-2,3-dimethyl-imidazolium-tetrafluoroborate; EMP-TFSI: 1-ethyl-1-methyl pyrrolidinium bis(trifluoromethane sulfonyl) imide; SN: Succinonitrile.

that most of these EDLCs are based on aqueous or organic liquid electrolytes except a few EDLCs, which are reported with polymer-based electrolytes [36,37]. The performance characteristics of the present solid-state EDLC cells are either comparable to or even better than many reported biomass-based EDLCs, even based on liquid electrolytes (Table 3).

For a comparison with earlier reports on similar carbon electrodes, the present pinecone-derived AC electrodes have been tested in an aqueous liquid electrolyte (6 M KOH). Symmetric EDLC cell has been assembled in two electrodes configuration, and EIS, CV and GCD patterns have been recorded, as shown in Fig.S6. All these studies demonstrate the typical capacitive nature of the present porous carbon electrodes in the liquid electrolyte (KOH). The values of specific capacitance, specific energy, maximum specific power and effective power have been evaluated and found to be  $\sim 299 \text{ F g}^{-1}$ ,  $\sim 15 \text{ Wh kg}^{-1}$ ,  $\sim 42 \text{ kW kg}^{-1}$  and  $257 \text{ W kg}^{-1}$ , respectively. In an earlier report [52], the pinecone-derived AC (activated by KOH) was tested in aqueous  $\text{Na}_2\text{SO}_4$  electrolyte, which showed lower specific capacitance ( $\sim 137 \text{ F g}^{-1}$ ). However, a slightly higher specific energy of  $19 \text{ Wh kg}^{-1}$  (at effective specific power of  $100 \text{ W kg}^{-1}$ ) has been reported as compared to the present AC-electrodes (Table 3). This has been observed primarily due to wider operating voltage range of the device assembled with  $\text{Na}_2\text{SO}_4$ -electrolyte. A high value of capacitance ( $277 \text{ F g}^{-1}$ ) and high specific energy ( $24.6 \text{ Wh kg}^{-1}$  at power density of  $400 \text{ W kg}^{-1}$ ) has been reported for pinecone AC electrode in KOH electrolyte for asymmetric capacitor with activated expanded graphite as cathode [53]. With non-aqueous liquid electrolyte 1 M  $\text{LiPF}_6$  in ethylene carbonate/dimethyl carbonate, AC electrodes derived from pinecone petals offer lower specific capacitance ( $142 \text{ F g}^{-1}$ ), however, the capacitor shows high specific energy of  $61 \text{ Wh kg}^{-1}$  (Table 3), as it could be charged for higher voltage range of 3.0 V [51]. This comparison confirms the suitability of present pinecone AC, activated by  $\text{ZnCl}_2$ , as EDLC electrodes with solid and flexible gel polymer electrolyte.

The variation of discharge specific capacitance ( $C_{ds}$ ) of the cells (Cell-1 and Cell-2) as a function of current densities is depicted in Fig. 8c. It has been noticed that the Cell-2 offers higher specific capacitance with respect to Cell-1 for each value of current density. Further, the Cell-2 shows relatively gradual decrease in specific capacitance with increasing current density compared to that of Cell-1, particularly in higher current density range. These observations confirm the moderately high rate capability of the porous activated carbon electrodes in the solid-state EDLC. As discussed earlier, the facile mobility of  $\text{Li}^+$  ions through porous carbon electrodes is responsible for high rate performance of the device. It has been specifically noted that the specific capacitance of both the cells decreases with faster rate for lower current densities up to  $\sim 10 \text{ A g}^{-1}$ . Thereafter, the gradual decrease in the capacitance has been observed for higher current densities (Fig. 8c). As mentioned earlier, the activated carbon electrodes has hierarchal porous texture possessing the mixture of micro- and mesoporosity. At lower current density, the higher capacitance is observed due to electrolyte ion switching through microporous interiors predominantly. On increasing the current, the electrolyte ions have limited accessibility to micropores, hence, a large proportion of surface area gets deprived of double layer formation and show a steep decrement in capacitance. On further increase in current density beyond  $\sim 10 \text{ A g}^{-1}$ , the fast ion switching through mesoporous interiors is responsible for slower decrease in capacitance in both the cells [84].

Fig. 8d compares the Ragone plots (i.e., specific energy,  $E$ , versus effective power density,  $P_{\text{eff}}$ ) of the two cells, Cell-1 (comprising GPE containing IL only) and Cell-2 (with GPE containing Li-salt dissolved in IL). The values of  $P_{\text{eff}}$  have been evaluated from:  $P_{\text{eff}} = E/t_0$ , where,  $t_0$  is discharge time of the cell after charging up to

1.5 V. The Ragone plots show the standard variations, which are generally observed for energy storage devices like EDLCs/supercapacitors [1–4,54]. A comparison of the two cells shows that the Cell-2 (with Li ions containing GPE) offers substantially higher value of the effective power as compared to that of Cell-1 at the same specific energy, particularly at higher current densities. As evident from the above mentioned studies also, the facile transport of  $\text{Li}^+$  ions through the suitable porous interiors of the activated carbon electrodes is important factor to obtain EDLC of high specific power. Fig. 8e demonstrates the glow of LED, connected with four units of EDLC cells (Cell-2, connected in series). The demonstration indicates that the system has capability to glow the LED (38–50 mW LED of 5 mm size) for long duration (about half an hour), indicating substantial energy stored by Cell-2.

The charge-discharge reversibility of the Cell-2 has been tested by charging and discharging the cell between 0 and 1.0 V at the current  $1.0 \text{ mA cm}^{-2}$  ( $1.4 \text{ A g}^{-1}$ ) for  $\sim 20,000$  cycles (Fig. 9). About 11% fading in discharge specific capacitance has been observed for initial few cycles followed by almost stable variation in capacitance with charge-discharge cycles up to  $\sim 20,000$  cycles. The initial fading is attributed to charge consumption due to some possible irreversible electrochemical (charge-transfer) reaction(s) with some species adsorbed on large surface area carbon electrodes at the interfaces [12,13]. In order to test the stability of the EDLC (Cell-2), EIS pattern has been recorded for the fresh cell and compared with the plots recorded after each interval of  $\sim 5000$  cycles, as shown in the inset of Fig. 9. The shapes of the EIS patterns are found to be almost unaltered, which confirm the stability of the cell with respect to charge-discharge cycles. Coulombic efficiency ( $\eta$ ) of the cell has been evaluated from the GCD patterns using the expression:  $\eta = \Delta t_D / \Delta t_C \times 100\%$ ; where  $\Delta t_C$  and  $\Delta t_D$  are time intervals for charge and discharge of the cell, respectively, at constant current for the same voltage range. The Cell-2 offers 96–100% Coulombic efficiency for  $\sim 20,000$  charge-discharge cycles, as shown in Fig. 9, which further confirms the stable cyclic performance of the cell.

### 3.3.4. Temperature dependent behavior of EDLC

Thermal stability of the EDLC cell (Cell-2) has been tested by recording EIS patterns at different temperatures, as illustrated in Fig. 10. The EIS patterns are found to be intact with only small deviations in the middle to high frequency range from  $-30$  to  $90^\circ\text{C}$  (Fig. 10a, inset). Fig. 10b depicts the variation of specific capacitance ( $C_s$ ) and bulk resistance  $R_b$  with respect to temperature. These observations indicate a thermally stable behavior of the EDLC cell for a wide temperature range from  $-30$  to  $90^\circ\text{C}$ . From thermal stability point of view, the present EDLC show comparable or even better

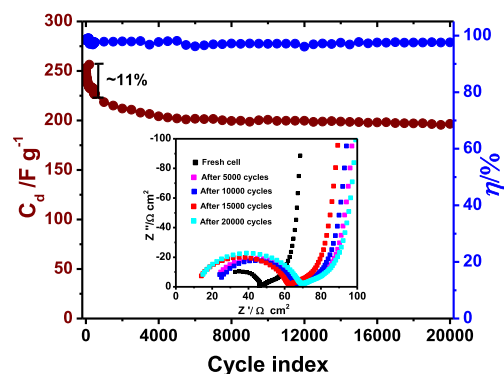
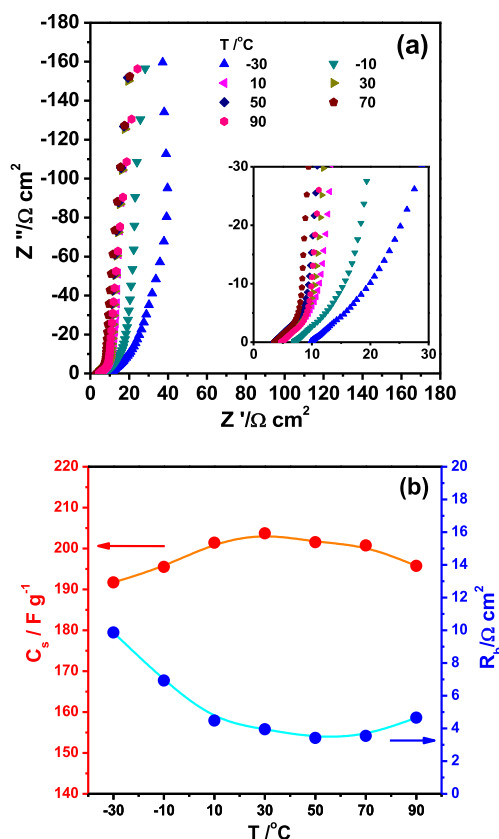


Fig. 9. Variation of specific discharge capacitance ( $C_{ds}$ ) and Coulombic efficiency ( $\eta$ ) as a function of charge-discharge cycles. The inset shows EIS plots, recorded after different intervals of cycles.





**Fig. 10.** (a) EIS plots of Cell-2 at different temperatures. The inset represents the expanded high frequency region, (b) variation of specific capacitance ( $C_s$ ) and cell resistance of the EDLC cell as a function of temperature.

performance compared to many recent reports on supercapacitors employing liquid electrolytes or GPEs [12,13,88,89]. A systematic study shows effect of organic solvents on the EDLCs' performance with temperature [88] and accordingly the solvent acetonitrile exhibits better performance than PC in the temperature range from  $-30$  to  $60$  °C. Capacitors based on GPE comprising succinonitrile and ionic liquid offer stable capacitance for wider temperature range as per recent report by Pandey et al. [89]. Our group recently reported flexible EDLC based on peanut-shell derived porous carbon electrodes and Mg-ion conducting GPE, which shows stable temperature dependent behavior for the temperature range from  $-50$  to  $70$  °C [13].

#### 4. Conclusions

Bio-waste pinecone has been found to be excellent source to produce porous activated carbon as EDLC electrode material, when carbonized and suitably activated employing proper proportion of activating agent  $\text{ZnCl}_2$ . Morphology/structure and nature of the porosity of AC powder are found to be highly dependent on the amount of  $\text{ZnCl}_2$ , used to activate the carbon powder. XRD studies indicate predominantly amorphous/disordered nature of the activated carbons. Defects and disorder in activated carbon have been observed at the microscopic level also, as indicated from Raman studies. Optimum surface area ( $1781 \text{ m}^2 \text{ g}^{-1}$ ) and largest proportion of mesoporosity, suitable for EDLC electrodes, have been observed in AC powder, which is produced taking 1:3 (w/w) ratio of pinecone powder and  $\text{ZnCl}_2$ . A gel polymer electrolyte comprising a mixture of non-ionic plastic crystal (SN) and OIPC (EMPTFSI), immobilised in PVdF-HFP has been found to be suitable electrolyte/

separator for the fabrication of solid-state and flexible EDLCs. Addition of Li-salt (LiTFSI) in GPE (PVdF-HFP/SN/EMPTFSI) has been found to play an important role in the improvement of EDLC's performance characteristics. The performance of EDLCs, fabricated with optimized porous AC electrodes and GPEs (without and with Li-salt), has been characterized by EIS, CV and galvanostatic charge-discharge measurements. A slight improvement in specific capacitance from  $\sim 244$  to  $\sim 255 \text{ F g}^{-1}$ , hence, in specific energy from  $\sim 19$  to  $\sim 20 \text{ Wh kg}^{-1}$  (as observed from charge-discharge tests) has been obtained, when Li-ion incorporated GPE is employed in EDLC. As observed from EIS studies, the EDLC cell with Li-salt containing GPE offers higher rate capability ( $\tau_o \approx 1.4 \text{ s}$  and  $P_o \approx 28.6 \text{ kW kg}^{-1}$ ) compared to the cell (with GPE without Li-salt) having  $\tau_o \approx 5.0 \text{ s}$  and  $P_o \approx 8.4 \text{ kW kg}^{-1}$ . This leads to high specific power of the cell ( $P_{\text{max}} \approx 55.7 \text{ kW kg}^{-1}$ ), as noted from charge-discharge studies. Almost stable cyclic performance of the EDLC cell has been obtained for  $\sim 20,000$  charge-discharge cycles after only  $\sim 11\%$  fading. High ionic conductivity of Li-salt containing GPE film and appropriate pore size distribution of highly disordered AC electrodes show synergistic effect to obtain high performance EDLC cells. The optimized EDLC cell (Cell-2) exhibits thermally stable performance in the temperature range between  $-30$  and  $90$  °C.

#### Acknowledgements

One of us (MYB) is thankful to Department of Science & Technology, New Delhi for providing fellowship under INSPIRE fellowship programme. Partial financial support, received from SERB, New Delhi (sanction order No.: EMR/2016/002197), is also thankfully acknowledged.

#### Appendix A. Supplementary data

Supplementary data to this article can be found online at <https://doi.org/10.1016/j.electacta.2019.02.092>.

#### References

- [1] L.L. Zhang, X.S. Zhao, Carbon-based materials as supercapacitor electrodes, *Chem. Soc. Rev.* 38 (2009) 2520–2531.
- [2] F. Beguin, E. Frackowiak, *Supercapacitors, Materials, Systems and Applications*, Wiley-VCH Verlag, Weinheim, Germany, 2009.
- [3] P. Simon, T. Brousse, F. Favier, *Supercapacitors Based on Carbon or Pseudocapacitive Materials*, Wiley, Hoboken, NJ, USA, 2017.
- [4] A. González, E. Goikolea, J.A. Barrena, R. Mysyk, Review on supercapacitors: technologies and materials, *Renew. Sustain. Energy Rev.* 58 (2016) 1189–1206.
- [5] S.A. Hashmi, Supercapacitor: an emerging power source, *Sci. Lett.* 27 (2014) 27–46.
- [6] M. Biswal, A. Banerjee, M. Deo, S. Ogale, From dead leaves to high energy density supercapacitors, *Energy Environ. Sci.* 6 (2013) 1249–1259.
- [7] A. Alabadi, X. Yang, Z. Dong, Z. Li, B. Tan, Nitrogen-doped activated carbons derived from a co-polymer for high supercapacitor performance, *J. Mater. Chem. A* 2 (2014) 11697–11705.
- [8] J. Wang, S. Kaskel, KOH activation of carbon-based materials for energy storage, *J. Mater. Chem.* 22 (2012) 23710–23725.
- [9] L. Wei, G. Yushin, Nanostructured activated carbons from natural precursors for electrical double layer capacitors, *Nanomater. Energy* 1 (2012) 552–565.
- [10] C. Peng, X. Yan, R. Wang, J. Lang, Y. Ou, Q. Xue, Promising activated carbons derived from waste tea-leaves and their application in high performance supercapacitors electrodes, *Electrochim. Acta* 87 (2013) 401–408.
- [11] R. Wang, P. Wang, X. Yan, J. Lang, C. Peng, Q. Xue, Promising porous carbon derived from celctue leaves with outstanding supercapacitance and  $\text{CO}_2$  capture performance, *ACS Appl. Mater. Interfaces* 4 (2012) 5800–5806.
- [12] N. Yadav, K. Mishra, S.A. Hashmi, Optimization of porous polymer electrolyte for quasi-solid-state electrical double layer supercapacitor, *Electrochim. Acta* 235 (2017) 570–582.
- [13] N. Yadav, M.K. Singh, N. Yadav, S.A. Hashmi, High performance quasi-solid-state supercapacitors with peanut-shell derived porous carbon, *J. Power Sources* 402 (2018) 133–146.
- [14] R.L. Zornitta, P. Srimuk, J. Lee, B. Krener, M. Aslan, L.A.M. Ruotolo, V. Presser, Charge and potential balancing for optimized capacitive deionization using lignin-derived, low-cost activated carbon electrodes, *ChemSusChem* 11

- (2018) 2101–2113.
- [15] D. Chernysheva, Y. Chus, V. Klushin, T. Lastovina, L. Pudova, N. Smirnova, O. Kravchenko, V. Chernyshev, V.P. Ananikov, Sustainable utilization of biomass refinery wastes for accessing activated carbons and supercapacitor electrode materials, *ChemSusChem* doi: 10.1002/cssc.201801757.
  - [16] W. Lu, L. Dai, in: *Carbon Nanotubes*, Jose Mauricio Marulanda, InTech, 2010, <https://doi.org/10.5772/39444>.
  - [17] G.P. Pandey, S.A. Hashmi, Y. Kumar, Multiwalled carbon nanotube electrodes for electrical double layer capacitors with ionic liquid based gel polymer electrolytes, *J. Electrochem. Soc.* 157 (2009) A105–A114.
  - [18] J. Li, X. Wang, Q. Huang, S. Gamboa, P.J. Sebastian, Studies on preparation and performances of carbon aerogel electrodes for the application of supercapacitor, *J. Power Sources* 158 (2006) 784–788.
  - [19] H. An, Y. Wang, X. Wang, L. Zheng, X. Wang, L. Yi, Polypyrrole/carbon aerogel composite materials for supercapacitor, *J. Power Sources* 195 (2010) 6964–6969.
  - [20] Z. Li, Z. Xu, X. Tan, H. Wang, C.M.B. Holt, T. Stephenson, B.C. Olsen, D. Mitlin, Mesoporous nitrogen-rich carbons derived from protein for ultra-high capacity battery anodes and supercapacitors, *Energy Environ. Sci.* 6 (2009) 871–878.
  - [21] L.F. Chen, X.D. Zhang, H.W. Liang, M. Kong, Q.F. Guan, P. Chen, Synthesis of nitrogen-doped porous carbon nanofibers as an efficient electrode material for supercapacitors, *ACS Nano* 6 (2012) 7092–7102.
  - [22] Y. Korenblit, M. Rose, E. Kockrick, L. Borchardt, A. Kvit, S. Kaskel, High-rate electrochemical capacitors based on ordered mesoporous silicon carbide-derived carbon, *ACS Nano* 4 (2010) 1337–1344.
  - [23] P. Simon, Y. Gogotsi, Materials for electrochemical capacitors, *Nat. Mater.* 7 (2008) 845–854.
  - [24] M.K. Singh, M. Suleman, Y. Kumar, S.A. Hashmi, A novel configuration of electrical double layer capacitor with plastic crystal-based gel polymer electrolyte and graphene nano-platelets as electrodes: a high rate performance, *Energy* 80 (2015) 465–473.
  - [25] M. Suleman, Y. Kumar, S.A. Hashmi, High-rate supercapacitive performance of GO/r-GO electrodes interfaced with plastic-crystal-based flexible gel polymer electrolyte, *Electrochim. Acta* 182 (2015) 995–1007.
  - [26] Q. Ke, J. Wang, Graphene-based materials for supercapacitor electrodes – a review, *J. Mater. Chem.* 2 (2016) 37–54.
  - [27] X. Shi, S. Zheng, Z.-S. Wu, X. Bao, Recent advances of graphene-based materials for high-performance and new-concept supercapacitors, *J. Energy Chem.* 27 (2018) 25–42.
  - [28] T. Kawano, M. Kubota, S. Maurice Onyango, F. Watanabe, H. Matsuda, Preparation of activated carbon from petroleum coke by KOH chemical activation for adsorption heat pump, *Appl. Therm. Eng.* 28 (2008) 865–871.
  - [29] E. Raymundo-Pinero, D. Cazorla-Amoros, A. Linares-Solano, J. Find, U. Wild, R. Schlogl, Structural characterization of N-containing activated carbon fibers prepared from a low softening point petroleum pitch and a melamine resin, *Carbon* 40 (2002) 597–608.
  - [30] P. Chingombe, B. Saha, R.J. Wakeman, Surface modification and characterization of a coal-based activated carbon, *Carbon* 43 (2005) 3132–3143.
  - [31] L. Gao, F.-Q. Dong, Q.-W. Dai, G.-Q. Zong, U. Halik, D.-J. Lee, Coal tar residues based activated carbon: preparation and characterization, *J. Taiwan Inst. Chem. Eng.* 63 (2016) 166–169.
  - [32] M.R. Jisha, Y.J. Hwang, J.S. Shin, N.K. Suk, T.P. Kumar, K. Karthikeyan, et al., Electrochemical characterization of supercapacitors based on carbons derived from coffee shells, *Mater. Chem. Phys.* 115 (2009) 33–39.
  - [33] L. Xiao, X. Wei, Z. Shuping, Z. Jin, L. Feng, Q.S. Zhang, et al., Preparation of capacitor's electrode from sunflower seed shell, *Bioresour. Technol.* 102 (2011) 1118–1123.
  - [34] M. Olivares-Marín, J.A. Fernández, M.J. Lázaro, C. Fernández-González, A. Macías-García, V. Gómez-Serrano, F. Stoeckli, T.A. Centeno, Cherry stones as precursor of activated carbons for supercapacitors, *Mater. Chem. Phys.* 14 (2009) 323–327.
  - [35] Z. Shuo, W. Cheng-Yang, C. Ming-Ming, W. Jin, S. Zhi-Qiang, Potato starch-based activated carbon spheres as electrode material for electrochemical capacitor, *J. Phys. Chem. Solid* 70 (2009) 1256–1260.
  - [36] M. Suleman, Y. Kumar, S.A. Hashmi, Flexible electric double-layer capacitors fabricated with micro-/mesoporous carbon electrodes and plastic crystal incorporated gel polymer electrolytes containing room temperature ionic liquids, *J. Solid State Electrochem.* 19 (2015) 1347–1357.
  - [37] A. Jain, S.K. Tripathi, Almond shell-based activated nanoporous carbon electrode for EDLCs, *Ionics* 21 (2015) 1391–1398.
  - [38] E. Raymundo-Pinero, M. Cadek, F. Beguin, Tuning carbon materials for supercapacitors by direct pyrolysis of seaweeds, *Adv. Funct. Mater.* 19 (2009) 1032–1039.
  - [39] Y. Qu, Y. Tian, B. Zou, J. Zhang, Y. Zheng, L. Wang, Y. Li, C. Rong, Z. Wang, A novel mesoporous lignin/silica hybrid from rice husk produced by a sol-gel method, *Bioresour. Technol.* 101 (2010) 8402–8405.
  - [40] D. Kalpana, S.H. Cho, S.B. Lee, Y.S. Lee, R. Misra, N.G. Renganathan, Recycled waste paper—a new source of raw material for electric double-layer capacitors, *J. Power Sources* 190 (2009) 587–591.
  - [41] Y.J. Kim, B.J. Lee, H. Suezaki, T. Chino, Y. Abe, T. Yanagiura, Preparation and characterization of bamboo-based activated carbons as electrode materials for electric double layer capacitors, *Carbon* 44 (2006) 1592–1594.
  - [42] L. Wei, M. Sevilla, A.B. Fuertes, R. Mokaya, G. Yushin, Hydrothermal carbonization of abundant renewable natural organic chemicals for high performance supercapacitor electrodes, *Adv. Energy Mater.* 1 (2011) 356–361.
  - [43] A.R. Mohamed, M. Mohammadi, G.N. Darzi, Preparation of carbon molecular sieve from lignocellulosic biomass: a review, *Renew. Sustain. Energy Rev.* 14 (2010) 1591–1599.
  - [44] D. Vamvuka, Bio-oil, solid and gaseous biofuels from biomass pyrolysis processed: an overview, *Int. J. Energy Res.* 35 (2011) 835–862.
  - [45] [https://en.wikipedia.org/wiki/Pinus\\_wallichiana](https://en.wikipedia.org/wiki/Pinus_wallichiana).
  - [46] N. Ayrlimis, U. Buyuksari, E. Avci, E. Koc, Utilization of pine (*Pinus pinea* L.) cone in manufacture of wood-based composite, *For. Ecol. Manage.* 259 (2009) 65–70.
  - [47] J.A. Micales, J.S. Han, J.L. Davis, R.A. Young, Chemical composition and fungitoxic activities of pine cone extracts, in: *Mycotoxins, Wood Decay, Plant Stress, Biocorrosion, Gen. Biodeterior*, Springer, Boston MA, 1994, pp. 317–332.
  - [48] G.V. Nunell, M.E. Fernandez, P.R. Bonelli, A.L. Cukierman, Nitrate uptake improvement by modified activated carbons developed from two species of pine cones, *J. Colloid Interface Sci.* 440 (2015) 102–108.
  - [49] A.E. Ofomaja, E.B. Naidoo, Biosorption of copper from aqueous solution by chemically activated pine cone: a kinetic study, *Chem. Eng. J.* 175 (2011) 260–270.
  - [50] A. Özhan, Ö. Şahin, M.M. Küçük, C. Saka, Preparation and characterization of activated carbon from pine cone by microwave-induced ZnCl<sub>2</sub> activation and its effects on the adsorption of methylene blue, *Cellulose* 21 (2014) 2457–2467.
  - [51] K. Karthikeyan, S. Amaresh, S.N. Lee, X. Sun, V. Aravindan, Y.-G. Lee, Y.S. Lee, Construction of high-energy-density supercapacitors from pine-cone-derived high-surface-area carbons, *ChemSusChem* 7 (2014) 1435–1442.
  - [52] F. Barzegar, A. Bello, J.K. Dangbegnon, N. Manyala, X. Xia, Asymmetric carbon supercapacitor with activated expanded graphite as cathode and Pinecone tree activated carbon as anode materials, *Energy Procedia* 105 (2017) 4098–4103.
  - [53] A. Bello, N. Manyala, F. Barzegar, A.A. Khaleed, Y. Damilola Momodua, J.K. Dangbegnon, Renewable pine cone biomass derived carbon materials for supercapacitor application, *RSC Adv* 6 (2016) 1800–1809.
  - [54] B.E. Conway, *Electrochemical Supercapacitors: Scientific Fundamentals and Technological Applications*, Kluwer Academic Plenum, New York, 2009.
  - [55] G. Wang, L. Zhang, J. Zhang, A review of electrode materials for electrochemical supercapacitors, *Chem. Soc. Rev.* 41 (2012) 797–828.
  - [56] R.C. Agrawal, G.P. Pandey, Materials designing and all-solid-state battery applications: an overview, *J. Phys. D: Appl. Phys.* 41 (2008) 223001.
  - [57] C. Zhao, W. Zheng, A review for aqueous electrochemical supercapacitors, *Front. Energy Res.* 3 (2015). Article 23.
  - [58] C. Zhong, Y. Deng, W. Hu, J. Qiao, L. Zhang, J. Zhang, A review of electrolyte materials and compositions for electrochemical supercapacitors, *Chem. Soc. Rev.* 44 (2015) 7484–7539.
  - [59] A. Eftekhari, Supercapacitors utilising ionic liquids, *Energy Storage Mater* 9 (2017) 47–69.
  - [60] V.L. Martins, R.M. Torresi, Ionic liquids in electrochemical energy storage, *Curr. Opin. Electrochem.* 12 (2018) 26–32.
  - [61] X. Cheng, J. Pan, Y. Zhao, M. Liao, H. Peng, Gel polymer electrolytes for electrochemical energy storage, *Adv. Energy Mater.* 8 (2018) 1702184.
  - [62] L. Xia, L. Yu, D. Hua, Z. George, Z. Chen, Electrolytes for electrochemical energy storage, *Mater. Chem. Front.* 1 (2017) 584–618.
  - [63] G.P. Pandey, Y. Kumar, S.A. Hashmi, Ionic liquid incorporated polymer electrolytes for supercapacitor application, *Indian J. Chem.* 49A (2010) 743–751.
  - [64] D.R. MacFarlane, M. Forsyth, Plastic crystal electrolyte materials: new perspectives on solid state ionics, *Adv. Mater.* 13 (2001) 957–966.
  - [65] J.M. Pringle, P.C. Howlett, D.R. MacFarlane, M. Forsyth, Organic ionic plastic crystals: recent advances, *J. Mater. Chem.* 20 (2010) 2056–2062.
  - [66] S. Long, D.R. MacFarlane, M. Forsyth, Ionic conduction in doped Succinonitrile, *Solid State Ionics* 175 (2004) 733–738.
  - [67] M. Suleman, Y. Kumar, S.A. Hashmi, Structural and electrochemical properties of succinonitrile-based gel polymer electrolytes: role of ionic liquid addition, *J. Phys. Chem. B* 117 (2013) 7436–7443.
  - [68] P.J. Alarco, Y. Abu-Lebdeh, A. Abouimrane, M. Armand, The plastic-crystalline phase of succinonitrile as a universal matrix for solid-state ionic conductors, *Nat. Mater.* 3 (2004) 476–481.
  - [69] L.-Z. Fan, J. Maier, Composite effects in poly (ethylene oxide)–succinonitrile based all-solid electrolytes, *Electrochem. Commun.* 8 (2006) 1753–1756.
  - [70] L.Z. Fan, X.-L. Wang, F. Long, All-solid-state polymer electrolyte with plastic crystal materials for rechargeable lithium-ion battery, *J. Power Sources* 189 (2009) 775–778.
  - [71] M. Patel, K.G. Chandrappa, A.J. Bhattacharyya, Increasing ionic conductivity of polymer–sodium salt complex by addition of a non-ionic plastic crystal, *Solid State Ionics* 181 (2010) 844–848.
  - [72] S. Li, K. Yang, Z. Zhang, L. Yang, S.-I. Hirano, Organic ionic plastic crystal–polyethylene oxide solid polymer electrolytes: application in all-solid-state lithium batteries, *Ind. Eng. Chem. Res.* DOI: 10.1021/acs.iecr.8b01964.
  - [73] Q. Li, J. Zhao, B. Sun, B. Lin, L. Qiu, Y. Zhang, X. Chen, J. Lu, F. Yan, High-temperature solid-state dye-sensitized solar cells based on organic ionic plastic crystal electrolytes, *Adv. Mater.* 24 (2012) 945–950.
  - [74] H. Marsh, F. Rodriguez-Reinonso, *Activated Carbon*, Elsevier Science & Technology Books, Amsterdam, 2006.
  - [75] Z. Hu, M.P. Srinivasan, Y. Ni, Preparation of mesoporous high-surface-area

- activated carbon, *Adv. Mater.* 12 (2000) 62–65.
- [76] A. Krause, P. Kossyrev, M. Oljaca, S. Passerini, M. Winter, A. Balducci, Electrochemical double layer capacitor and lithium-ion capacitor based on carbon black, *J. Power Sources* 196 (2011) 8836–8842.
- [77] S.T. Senthilkumar, R.K. Selvan, J.S. Melo, C. Sanjeeviraja, High performance solid-state electric double layer capacitor from redox mediated gel polymer electrolyte and renewable tamarind fruit shell derived porous carbon, *ACS appl. Mater. Inter.* 21 (2013) 10541–10550.
- [78] Z.Q. Li, C.J. Lu, Z.P. Xia, Y. Zhou, Z. Luo, X-ray diffraction patterns of graphite and turbostratic carbon, *Carbon* 45 (2007) 1686–1695.
- [79] J.R. Miller, 8th International Seminar on Double Layer Capacitor and Similar Energy Storage Devices, 1998, Deerfield Beach Florida (1998).
- [80] P.-L. Taberna, P. Simon, J.F. Fauvarque, Electrochemical characteristics and impedance spectroscopy studies of carbon-carbon supercapacitors, *J. Electrochem. Soc.* 150 (2003) A292–A300.
- [81] C.F. Liu, Y.-C. Liu, T.-Y. Yi, C.-C. Hu, Carbon Materials for High-Voltage Supercapacitors, *Carbon* (2018), <https://doi.org/10.1016/j.carbon.2018.12.009>.
- [82] L. Cheng, P. Guo, R. Wang, L. Ming, F. Leng, H. Li, X.S. Zhao, Electrocapacitive properties of supercapacitors based on hierarchical porous carbons from chestnut shell, *Colloids Surf. A* 446 (2014) 127–133.
- [83] T.E. Rufford, D. Hulicova-Jurcakova, Z. Zhu, G.Q. Lu, Nanoporous carbon electrode from waste coffee beans for high performance supercapacitors, *Electrochem. Commun.* 10 (2008) 1594–1597.
- [84] A.E. Ismanto, S. Wang, F.E. Soetaredjo, S. Ismadji, Preparation of capacitor's electrode from cassava peel waste, *Bioresour. Technol.* 101 (2010) 3534–3540.
- [85] Y. Jing, Y. Liu, X. Chen, Z. Hu, G. Zhao, Carbon electrode material with high densities of energy and power, *Acta Phys. - Chim. Sin.* 24 (2008) 13–19.
- [86] M.S. Balathanigaimani, S. Wang-Geun, L. Min-Joo, K. Chan, L. Jae-Wook, M. Hee, Highly porous electrodes from novel corn grains-based activated carbons for electrical double layer capacitors, *Electrochem. Commun.* 10 (2008) 868–871.
- [87] J. Li, G. Zan, Q. Wu, Nitrogen and sulfur self-doped porous carbon from brussel sprouts as electrode materials for high stable supercapacitors, *RSC Adv.* 6 (2016) 57464–57472.
- [88] M. Arulepp, L. Permann, J. Leis, A. Perkson, K. Rumma, A. Jänes, E. Lust, Influence of the solvent properties on the characteristics of a double layer capacitor, *J. Power Sources* 133 (2004) 320–328.
- [89] G.P. Pandey, T. Liu, C. Hancock, Y. Li, X.S. Sun, J. Li, Thermostable gel polymer electrolyte based on succinonitrile and ionic liquid for high-performance solid-state supercapacitors, *J. Power Sources* 328 (2016) 510–519.